J. Fluid Mech. (1995), *vol.* 288, *pp.* 265–310

The flow behind rings: bluff body wakes without end effects

By T. LEWEKE AND M. PROVANSAL

Laboratoire de Recherche en Combustion, URA 1117 CNRS/Université de Provence,
Faculté de Saint-Jérôme, Service 252, F-13397 Marseille Cédex 20, France

(Received 28 March 1994 and in revised form 17 November 1994)

Recent studies have demonstrated the strong influence of end effects on low-Reynolds-number bluff body wakes, and a number of questions remain concerning the intrinsic nature of three-dimensional phenomena in two-dimensional configurations. Some of them are answered by the present study which investigates the wake of bluff rings (i.e. bodies *without* ends) both experimentally and by application of the phenomenological Ginzburg–Landau model. The model turns out to be very accurate in describing qualitative and quantitative observations in a large Reynolds number interval. The experimental study of the periodic vortex shedding regime shows the existence of discrete shedding modes, in which the wake takes the form of parallel vortex rings or 'oblique' helical vortices, depending on initial conditions. The Strouhal number is found to decrease with growing body curvature, and a global expression for the Strouhal–Reynolds number relation, including curvature and shedding angle, is proposed, which is consistent with previous straight cylinder results. A secondary instability of the helical modes at low Reynolds numbers is discovered, and a detailed comparison with the Ginzburg–Landau model identifies it as the Eckhaus modulational instability of the spanwise structure of the near-wake formation region. It is independent of curvature and its clear observation in straight cylinder wakes is inhibited by end effects.

The dynamical model is extended to higher Reynolds numbers by introducing variable parameters. In this way the instability of periodic vortex shedding which marks the beginning of the transition range is characterized as the Benjamin–Feir instability of the coupled oscillation of the near wake. It is independent of the shear layer transition to turbulence, which is known to occur at higher Reynolds numbers. The unusual shape of the Strouhal curve in this flow regime, including the discontinuity at the transition point, is qualitatively reproduced by the Ginzburg–Landau model. End effects in finite cylinder wakes are found to cause important changes in the transition behaviour also: they create a second Strouhal discontinuity, which is not observed in the present ring wake experiments.

1. Introduction

The flow around bluff bodies, and especially the problem of an infinite circular cylinder placed in a uniform crossflow, has received considerable attention in the past, both from engineering and fundamental points of view. In the absence of analytical solutions for this conceptually simple problem, except for very low Reynolds numbers, most of the present knowledge comes from experimental and, more recently, numerical work.

The basic flow feature at low Reynolds numbers is the Bénard–von Kármán instability, i.e. the passage from stationary to oscillating flow with the formation of a regular 'vortex street' in the cylinder wake. Although this phenomenon has been known for over a hundred years, it is only recently that a decisive step in the understanding of the periodic vortex shedding regime has been made. From the studies of Williamson (1988*a*, 1989), Eisenlohr & Eckelmann (1990), König, Eisenlohr & Eckelmann (1989). Albarède, Provansal & Boyer (1990), Hammache & Gharib (1991), and others, it became clear that 'end effects' linked to the finite cylinder length in experiments had a strong influence on the whole wake, even for very long cylinders (hundreds of diameters). They were found to be responsible for a number of three-dimensional phenomena which had been observed in this nominally two-dimensionally configuration: oblique instead of parallel vortex shedding (see e.g. a discussion of 'older' results in Berger & Wille 1972), spanwise cells of different shedding frequencies (Gerich & Eckelmann 1982), vortex splitting (Eisenlohr & Eckelmann 1989) and vortex dislocations (Williamson 1989, 1992). Furthermore Williamson (1989) showed that the frequently observed discontinuities in the Strouhal–Reynolds number relationship (Strouhal number being the non-dimensional shedding frequency), were directly related to these three-dimensional phenomena, thus ending a thirty-year long debate on the reality and the causes of such discontinuities in a 'clean' experiment (Tritton 1959, 1971; Gaster 1969, 1971; Gerrard 1978; Sreenivasan 1985; Van Atta & Gharib 1987; and others). When the end conditions are controlled to produce parallel shedding, the same Strouhal curve (within 1 %) which is continuous in the entire periodic vortex shedding range, has now been found by many experimentalists, in agreement with two-dimensional numerical simulations (Karniadakis & Triantafyllou 1989). A review of these recent results can be found in Williamson (1995).

Typical cylinder end configurations in experiments, such as end plates (angled or not) (Williamson 1989), coaxial end cylinders of bigger diameter (Eisenlohr & Eckelmann 1989), perpendicular control cylinders upstream (Hammache & Gharib 1989), or simply the wind tunnel walls, all introduce large-scale perturbations like vortex dislocations, spanwise end cells of lower shedding frequency and complicated vortex reconnections. Even the rather 'clean' method of end suction, devised recently by Miller & Williamson (1994), still represents an external manipulation of the flow, and the condition that the flow oscillation has to seize near the ends of the cylinder still imposes an important constraint.

It is therefore desirable to somehow get rid of these conventional end boundary conditions. This requirement is fulfilled in the wake of a torus, i.e. a ring with circular cross-section, a body with a spanwise periodicity but without ends, which is the subject of the present paper. For sufficiently large aspect ratios (ring perimeter/cross-section diameter) the additional effects of body curvature are expected to be small and the wake should behave very nearly like the wake of a straight circular cylinder subject to periodic boundary conditions in the spanwise direction. This is confirmed in the present study.

Despite the fact that the choice of this configuration seems quite natural, it has received very little attention in the past, compared to the straight circular cylinder. Very preliminary measurements of the vortex shedding frequencies in the laminar wake of rings were made by Roshko (1953), who found that they were lower than for circular cylinders by a few percent. He also noticed a drastic change in the shape of the Strouhal curves for very low aspect ratios. This was confirmed by the measurements of Takamoto (1987) and Bearman & Takamoto (1988) for Reynolds numbers around 10^4 and rings of non-circular cross-section, which showed that, for aspect ratios lower than about 20, the ring wake behaved more like the wake of a solid disk, while for greater values its appearance was locally close to that of a straight cylinder wake. They also showed visualizations of the vortex street behind rings at low Reynolds numbers, made up of counter-rotating vortex rings (see also Takamoto & Izumi 1981). It was Monson (1965, 1981, 1983) who first showed that this is not the only possible ring wake configuration, by visualizing two counter-rotating helical vortices in the wake of high-aspect-ratio rings in free fall in a viscous fluid. He was mainly concerned with drag characteristics, and his measurements of the Strouhal number, rather difficult in his set-up, are not conclusive. All experiments on ring wakes show that the vortex street geometry is slightly modified by curvature effects. Instead of being equally spaced, as in the case of a straight body, the inner and outer vortices in a ring wake tend to 'pair', owing to their self-induced velocity. This phenomenon and its influence on the shedding frequency is further discussed in this paper.

Two other studies may be mentioned in this context. The first is a three-dimensional numerical simulation by Rivet (1991) of a straight circular cylinder wake with periodic boundary conditions, using a lattice gas algorithm. Starting from random noise, he observes the development of an oblique vortex street corresponding to a helical wake. In the second, Ehrhardt (1979) performs an inviscid linear stability analysis of a street of counter-rotating ring vortices, but with unrealistic assumptions about the circulation and geometry of the vortex configuration. His visualizations are similar to the ones shown by Takamoto (1987).

Thus the present investigation represents the first systematic study of the wakes behind high-aspect-ratio rings at low Reynolds numbers. Concerning the periodic vortex shedding regime discussed at the beginning, it shows which of the three-dimensional phenomena are intrinsic, i.e. not caused by end effects. Furthermore, new phenomena (instability of oblique vortex shedding and mode transitions at low Reynolds numbers), which are normally inhibited or hidden by the influence of the end conditions, are discovered and characterized by quantitative measurements.

This work also covers aspects of the so-called transition range, for Reynolds numbers just above the periodic regime. Even for straight circular cylinders, the phenomena in this region are not clearly understood and little detailed experimental data is available. In the transition range, which for circular cylinders was identified and described for the first time by Roshko (1953), the periodic vortex shedding becomes unstable and the wake fluctuations become rather irregular. Since the first signs of the transition to turbulence in the near wake, in the form of high-frequency transition waves in the separated shear layers, appear only at much higher Reynolds numbers (see e.g. Bloor 1964), this transition is generally attributed to a three-dimensional (spanwise) instability of the vortex formation process, based on visualization studies of Hama (1957), Gerrard (1978), and, in more detail, Williamson (1992). This spanwise near-wake instability is also found in the numerical simulations of Karniadakis & Triantafyllou (1992) and the stability analysis of Noack, König & Eckelmann (1993), but its physical origin is still not clear.

When increasing the Reynolds number through the transition range, Williamson (1991) observed two discontinuities in the Strouhal curve representing the dominating frequencies in the wake of a finite cylinder. He associated the different branches of this curve to different modes of vortex shedding, which was supported by his visualization studies. In this paper we investigate if and how the transitions between these modes, and the corresponding Strouhal discontinuities, are affected by end effects.

In addition to the purely experimental approach, the ring wake is also studied using a dynamical wake model involving a Ginzburg–Landau amplitude equation. It has been shown experimentally by Mathis, Provansal & Boyer (1984), and subsequently by

Provansal, Mathis & Boyer (1987), Sreenivasan, Strykowski & Ohlinger (1986), and Schumm, Berger & Monkewitz (1994), that the vortex street wake represents a limit-cycle oscillation of the entire flow, which is the saturated result of a time-amplified linear global instability (see Huerre & Monkewitz 1990 for a review on the concept of global oscillation modes). Transient experiments showed that temporal growth rates and nonlinear frequency variations do indeed not depend on the measuring point, which means that the dynamics of the entire two-dimensional wake can be described by a single Stuart–Landau equation. The parameters of this phenomenological model could be determined from experiments and the onset of vortex shedding was identified as a supercritical Hopf bifurcation with a change of sign of the temporal growth rate at the threshold. In order to incorporate three-dimensional phenomena, Albarède (1991) recently extended this model by adding a diffusive coupling in the spanwise direction. This leads to a Ginzburg–Landau equation, which is well known in the description of spatial patterns in closed systems, such as Rayleigh–Bénard convection or Taylor vortex flow (see the review by Cross & Hohenberg 1993). When applied to circular cylinders, the Ginzburg–Landau model is able to reproduce a great number of obsered three-dimensional wake dynamics, as shown by Albarède *et al.* (1990), Albarède & Monkewitz (1992), and Albarède & Provansal (1995). They also made quantitative comparisons with experimental data and deduced further parameters from the latter. Two-dimensional Ginzburg–Landau models also including the downstream direction have been studied by Park & Redekopp (1992) and Chiffaudel (1992), but the introduction of a streamwise term yielded no qualitatively new results. Here, the one-dimensional model of Albarède and co-workers is used to describe and understand the phenomena observed in the ring wake experiments.

Some preliminary results of the present study have been published recently. They concern the existence of different modes in ring wakes (Leweke, Provansal & Boyer 1993*a*), the observation of a new secondary instability of laminar vortex shedding (Leweke, Provansal & Boyer 1993*b*), as well as some features of the transition range and the Ginzburg–Landau model (Leweke & Provansal 1994*a*, *b*). Some of these results are included in the present paper, together with many further results, to give a coherent overview on ring wakes at low Reynolds numbers.

After a description of the experimental methods in §2, experimental results of the ring wake study are presented in §§3 and 4 for the periodic regime and the transition range respectively. In §5 the Ginzburg–Landau model is recalled and used in a qualitative and quantitative way to account for the phenomena observed in the periodic regime. In §6 the model is used to give a qualitative interpretation of the instability of periodic vortex shedding and some of the observations made in the transition range. A discussion and conclusions are given in §7.

2. Experimental details

The ring wakes were studied in an open-circuit low-speed wind tunnel with a 1 m long square test section (25 cm × 25 cm). The free stream turbulence level was close to 0.1 % and flow uniformity better than 0.5 % over 80 % of the tunnel width. Four rings, made of polished or nickel-coated brass, with different outer diameters D and cross-section diameters d were used, covering a range of aspect ratios $\pi D/d$ from 30 to 100. These are well above the limiting value found by Bearman & Takamoto (1988) below which a disk wake behaviour is observed. The non-dimensional curvature $K = 2d/D$, which in the case of a ring is equivalent to the aspect ratio, is also used in the following. The geometrical data are given in table 1. For comparison several straight circular

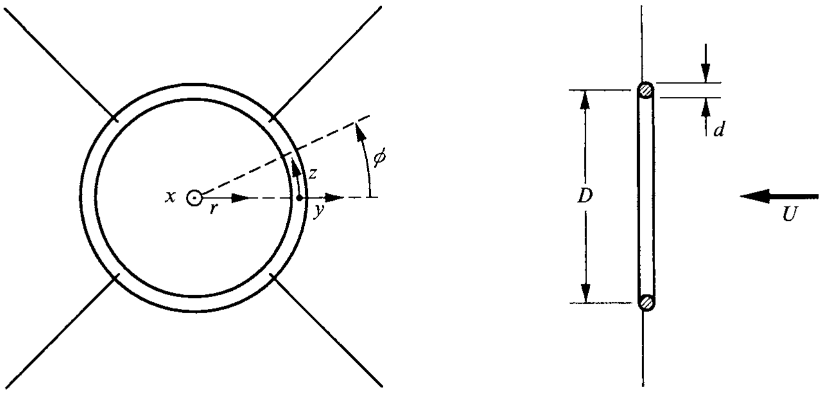

FIGURE 1. Bluff ring geometry and coordinate system. $y = r - D/2, z = \phi D/2$.

Rings	1	2	3	4
d (mm)	2.99	1.99	3.03	3.06
D (mm)	94.6	48.2	56.9	30.6
$\pi D/d$	99.5	76.2	59.0	31.5
K	0.0631	0.0825	0.106	0.199
Re_c	48.6	49.0	49.8	52.4
Observed modes	$-3,\ldots,+3$	$-3,\ldots,+3$	$-2,\ldots,+3$	$-1, 0, +1$
A	-3.681	-3.667	-3.683	-3.696
B	0.1875	0.1868	0.1874	0.1885
C	1.236×10^{-4}	1.278×10^{-4}	1.183×10^{-4}	0.986×10^{-4}

TABLE 1. Ring wake data concerning body geometry, the critical Reynolds number, the modes, and the Strouhal curve (3.5) of parallel shedding in the periodic regime.

cylinders with aspect ratios (length L/diameter d) between 80 and 120 were also used. To ensure parallel shedding in the periodic regimes, these steel cylinders were fitted either with angled end plates (Williamson 1989) or with end cylinders according to Eisenlohr & Eckelmann (1989).

The rings were held in a plane perpendicular to the flow at 15 m from the entry of the test section by four 0.08 mm diameter metal wires (see figure 1), which were fixed on a frame outside the test section and tightened by weights. The body-to-wire diameter ratio was 38 for three of the four rings and 25 for the remaining one. The wires were soldered into 0.5 mm holes at 135° from the front stagnation point of the ring cross-section in order to reduce the perturbation of the boundary layer. Alignment of the ring perpendicular to the flow with a precision better than 1° was possible using four micrometer screws at the wire ends.

A simple but sensitive laser-photo diode set-up was used to monitor the oscillations of the rings (1 V output per 1/100 mm displacement). Although oscillations were never completely absent, their amplitude remained well below 1 % of the body diameter d and were mainly longitudinal, i.e. in the direction of the flow. No influence on the amplitude or frequency of vortex shedding could be detected for any of the rings.

It soon became clear that, in certain Reynolds number intervals of the periodic regime, a number of different shedding modes, involving vortex rings and different helical vortices, were possible, depending on initial conditions (see §3.1). These modes were easily identified by the 'Lissajous' figures produced on an oscilloscope by the

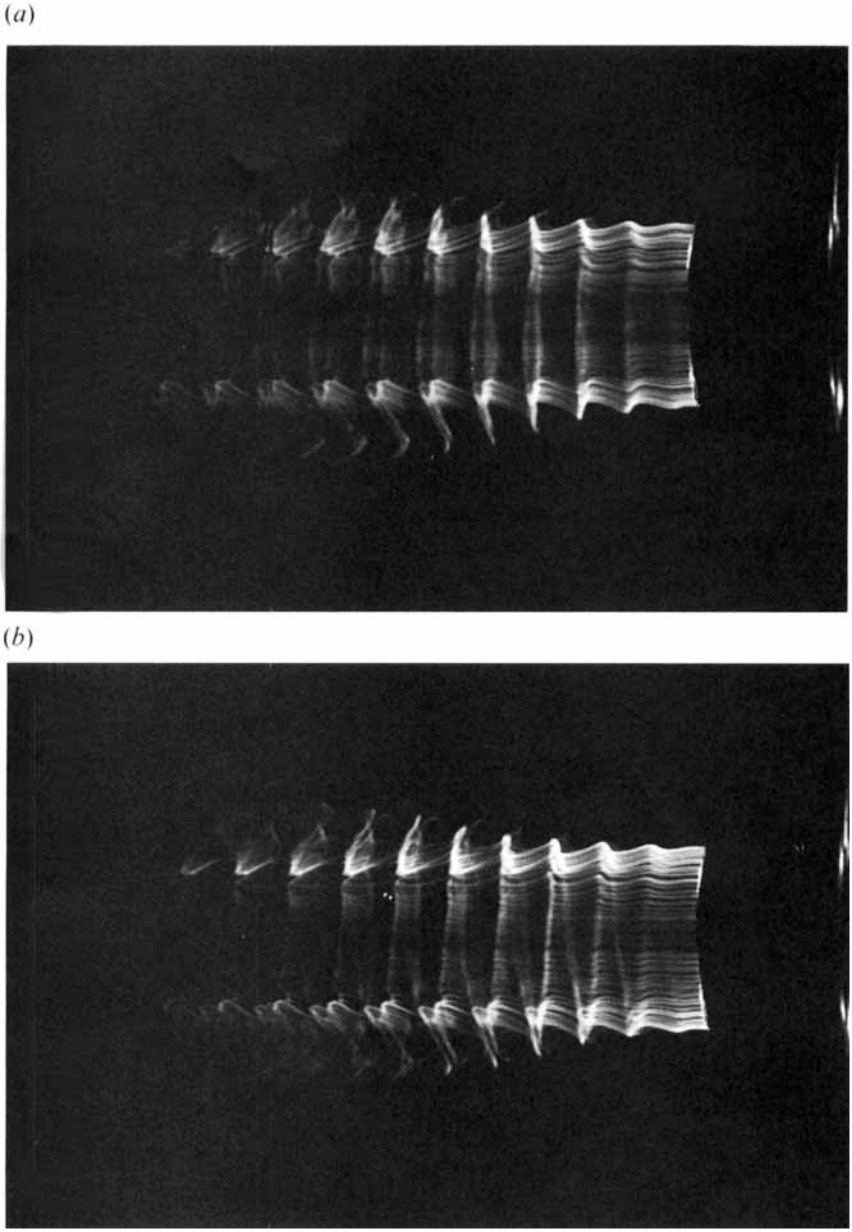

Figure 2(*a*, *b*). For caption see facing page.

outputs of two hot-wire sensors, placed at two fixed spanwise positions. Mode changes could be forced with reasonable repeatability by the following method. For a few seconds air under pressure was injected into the test section through a hole in the sidewall close to the plane of the ring. This violent perturbation destroyed the periodic wake and, depending on the transverse position of the jet, created a large-scale swirling flow in the test section, which served as a new initial condition for the ring wake.

The free stream velocity U was measured by laser Doppler anemometry (LDA) in the centre of the tunnel cross-section 50 mm upstream of the ring. Corrections were

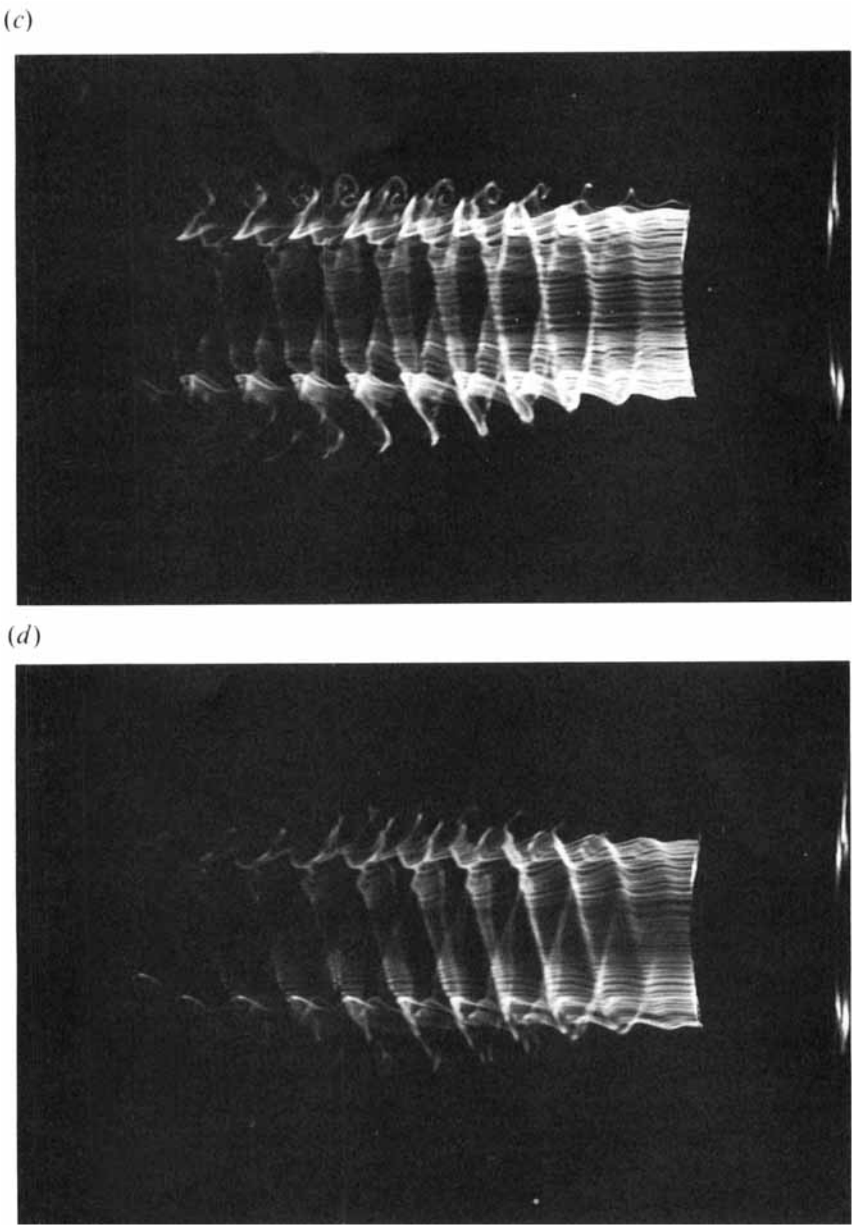

FIGURE 2. Visualizations of different ring wake structures at $Re = 105$, aspect ratio $\pi D/d = 76.2$. Flow is from right to left. The deformations of the cylindrical smoke sheet are visible as bright lines which correspond to isophase lines in the wake. They are formed by pairs of counter-rotating vortices, thus indicating their spatial structure: (*a*) closed vortex rings, (*b–d*) single, double, and triple helixes.

made for blockage effects and the downstream evolution of U due to wind tunnel boundary layer growth. This was necessary because of the very low velocities encountered at low Reynolds numbers. U is an important quantity because it enters into both the Reynolds and the Strouhal numbers. The statistical error in U, resulting from the geometric determination of the angle between two laser beams and a voltage readout is estimated at 0.3%. The kinematic viscosity ν was calculated from the temperature measured by a calibrated platinum resistance, with a statistical error of 0.1%. Velocity measurements in the wake were made using two standard hot-wire probes and a computer controlled mobile LDA point. Most measurements were made between $5d$ and $7d$ downstream of the body and 1–2 diameters off the local wake centreline.

A standard two-channel spectrum analyser, as well as an analogue phase meter, were used to obtain wake frequencies f (statistical error less than 0.1% in the periodic regime), spectra, correlation functions, or phase differences. The cross-section diameter of the rings was measured mechanically and the average of 20–30 measurements at different spanwise positions was taken for d (statistical error 0.2%).

For a given ring the statistical errors in Reynolds number $Re = Ud/\nu$ and Strouhal number of the laminar regime $S = fd/U$ are thus estimated at 0.4%. For the comparisons between rings 0.2 points have to be added. The additional systematic error may be of the same order, but it is likely to be the same for all measurements. The relevance of these error estimates becomes clearer in §3, where the differences between measured Strouhal curves are shown to be quite small.

Visualizations of the laminar ring wake structures were obtained using the smoke wire technique. A circular smoke wire, concentric with the ring, was placed at about 10 diameters downstream of the latter. It was held by two thin wires which also connected it to the output of an electric power supply. When painted with smoke oil and heated by an electric current, it produced a cylindrical smoke sheet which lasted for a few seconds.

More details about the experimental conditions can be found in Leweke (1994).

In the following, cylindrical coordinates (x, r, ϕ) as defined in figure 1 are used, with the origin at the centre of symmetry of the ring. With reference to cylinder experiments the local transverse and spanwise coordinates $y = r - D/2$ and $z = \phi D/2$ are also introduced.

3. Experimental results. I. The periodic regime

In this section experimental observations made in the wake of rings for Reynolds numbers between 50 and 200 approximately are described.

3.1. *Ring wake shedding modes*

The wake of a ring with high aspect ratio, i.e. small curvature, is locally very similar to the wake of a straight body. Therefore the ring can qualitatively be considered as a two-dimensional configuration with periodic boundary conditions. The phenomenon of oblique vortex shedding observed in periodic circular cylinder wakes would therefore also be expected here, but with only discrete shedding angles because of the boundary conditions. For the ring geometry this results in different helical structures. Figure 2 shows visualizations of four possible configurations in the wake of a ring with aspect ratio 76.2 at $Re = 105$. In figure 2(a) the vortices are closed rings parallel to the body. In figure 2(b–d) they form single, double, or triple helixes of different helix steps. It is important to realize that the lines visible in figure 2 are each formed by *two* counter-rotating vortices, and that, for example, the wake in figure 2(d) is made up of six interwoven helical vortices.

These modes can further be characterized by the spanwise evolution of the phase Φ of the periodic velocity fluctuations in the wake. At a given downstream and transverse position, these fluctuations are proportional to $\sin[2\pi ft + \Phi(z)]$ (when the harmonics are filtered), where t is time and f the wake or vortex shedding frequency. The phase

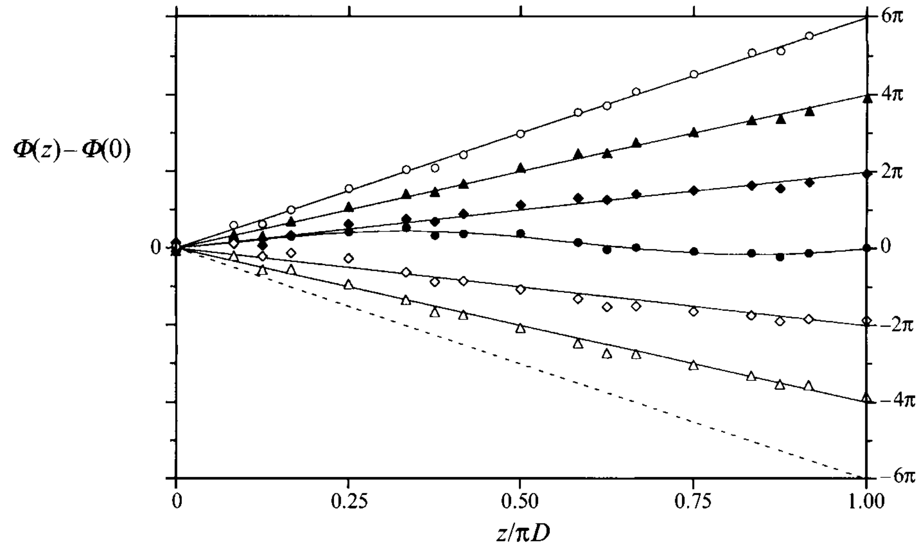

FIGURE 3. Phase difference of the periodic velocity fluctuations as function of spanwise position. Ring aspect ratio $\pi D/d = 59.0$, $Re = 127$. Wake modes $n = +3$ (○), $+2$ (▲), $+1$ (◆), 0 (●), -1 (◇), and -2 (△).

difference $\Delta\Phi = \Phi(z)-\Phi(0)$ was obtained for a series of spanwise positions from the correlation function of the simultaneous velocity signals from the mobile LDA point and a fixed hot wire at $z = 0$ serving as a phase reference. Figure 3 shows $\Delta\Phi$ for all the modes observed in the wake of the ring with $\pi D/d = 59.0$ at $Re = 127$. As expected, the phase is nearly linear in the spanwise coordinate for the helical 'oblique' modes. The almost sinusoidal phase variation of the vortex ring or 'parallel' mode results from a slight inclination of the vortex rings with respect to the body. This phenomenon, which is more pronounced at lower Reynolds numbers, was observed almost systematically. It is linked to small imperfections of the ring where the support wires are fixed. These variations are also present in the helical modes, but less visible because of the stronger underlying linear phase variation. An imporant quantity, which is used in §5, is the (mean) spanwise wavenumber $Q = \partial\Phi/\partial z$. For rings it takes discrete values $Q_n = 2n/D$, where n is an integer. It is independent of the streamwise wavelength, which is not true for the shedding angle (helix angle) frequently used to characterize oblique vortex shedding. In the following the modes are often referred to by their winding number n.

The visualizations in figure 2 (as well as the phase measurements in figure 3) were made with the same ring at the same Reynolds number, and each of the modes is perfectly stable, even robust: the wind tunnel sidewall could be opened and closed without 'losing' the mode. The domains of stability are shown in figure 4 for the same ring as in figure 3. They overlap in large intervals in Reynolds number. The upper limit marks the beginning of the transition range, which is discussed in §4. The higher helix modes have a tendency to remain stable longer than the lower order or parallel modes. The lower limit is associated with a secondary instability of the vortex shedding, shown in detail in §3.4.

The key to the selection of the mode which will be observed in a particular run is the initial conditions. In the present experiments they could be influenced by the method described in the previous section. When the oscillatory state was reached by increasing

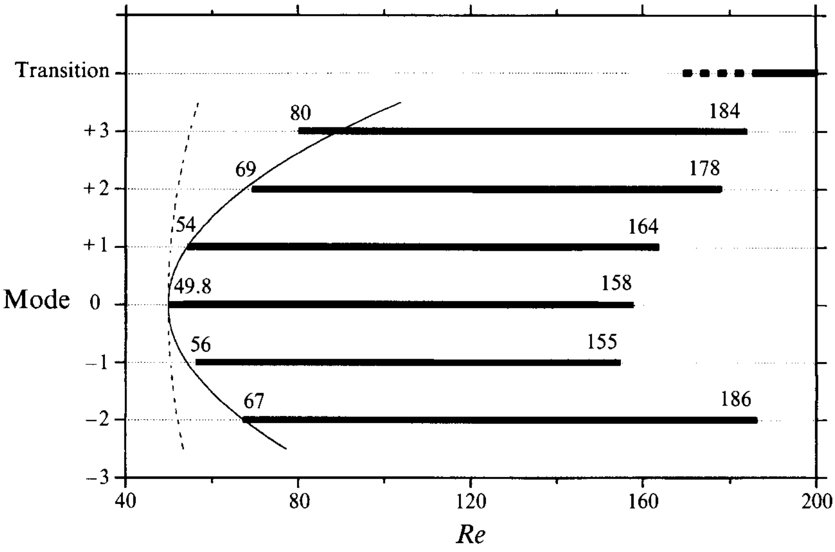

FIGURE 4. Stability domains of the periodic vortex shedding modes for the ring with aspect ratio $\pi D/d = 59.0$. For the thin lines, see §5.3.

the flow smoothly from rest or from subcritical conditions, the parallel mode was always selected. This can be explained by the fact that the flow acceleration is 'in phase' over the whole body span, and, according to figure 4, the parallel mode 0 also has the lowest stability limit. This is consistent with the observation that in towing tanks the shedding behind circular cylinders is always parallel just after the start of the motion, and it also explains why the helical modes have not been observed in the majority of the previous investigations of ring wakes. Whenever they appeared there had been some kind of messy initial condition. In his experimental study, Monson (1965) dropped the rings into the liquid, and Rivet (1991) started his numerical simulation from random noise. The present method to switch modes was motivated by these ideas. Its limitations, due to the random character of the perturbation, are illustrated by the fact that it was not possible to observe the mode $n = -3$ for the ring with $\pi D/d = 59.0$ (figures 3–7) or even higher-order helix modes, which could be expected for the rings with the highest aspect ratio.

3.2. *Strouhal numbers*

From circular cylinder investigations it is known that the vortex shedding frequency f is a function of the shedding angle θ, i.e. the angle between the vortices and the body. Williamson (1989) showed that the Strouhal number $S = fd/U$ at a given Reynolds number is given, to a very good approximation, by

$$S = S_0 \cos\theta, \tag{3.1}$$

where S_0 is the value for parallel shedding; the frequency decreases with increasing angle.

The same behaviour is observed in the torus wake. The Strouhal–Reynolds number curves have been determined for all the modes of a given ring, and the result for the one with $\pi D/d = 59.0$ is shown in figure 5. The downshift of the Strouhal curves for increasing wake winding numbers is clearly visible. Another important observation is the fact that the Strouhal curves for all the modes are continuous, and the wake

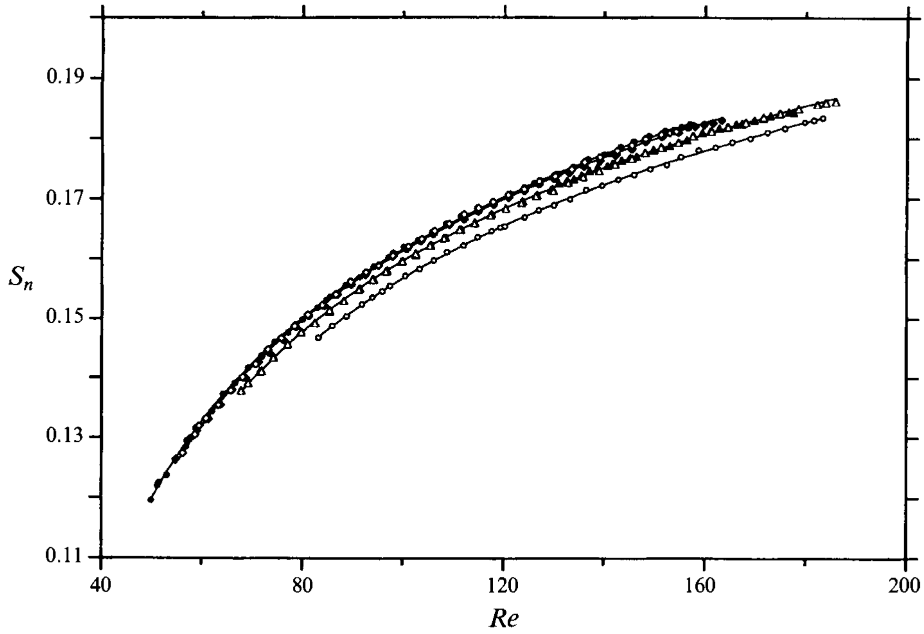

FIGURE 5. Strouhal number as function of Reynolds number and shedding mode for the ring with aspect ratio $\pi D/d = 59.0$. Symbols as in figure 3.

fluctuations are strictly periodic with a single frequency throughout the laminar regime. Phenomena such as spanwise cells of different frequencies, dislocations, or transitions between different oblique shedding angles do not occur (except at the limits of the stability domains, to be discussed further down). The continuity and smoothness also show that there is no lock-in effect from the interaction of flow and body oscillations.

In order to compare with (3.1), the angle θ is needed. For the ring, the discrete helix angles θ_n, which are the shedding angles in the developed plane of the wake, are used. It is easily seen that they are given by

$$\theta_n = \tan^{-1}|n|\,\lambda_n/\pi D, \tag{3.2}$$

where λ_n is the streamwise wavelength of mode n. Equation (3.1) and the fact that the vortex convection speed is nearly independent of the shedding angle imply that the wavelengths satisfy the relation $\lambda_n = \lambda_0/\cos\theta_n$ (Williamson 1989). Together with (3.2) this leads to an expression which is independent of θ_n:

$$\frac{\lambda_n}{d} = \frac{\lambda_0}{d}\left[1 - n^2\frac{(\lambda_0/d)^2}{(\pi D/d)^2}\right]^{-1/2}. \tag{3.3}$$

The wavelengths were measured by displacing the mobile LDA point in the streamwise direction and by determining the distance needed to reproduce a particular Lissajous figure from the LDA output and the signal from a fixed hot wire on an oscilloscope. The average of six wavelengths measured in an approximate interval $5d < x < 40d$ was taken. The results can be seen in figure 6, with the lines showing the functions (3.3). λ_0/d is given by a fourth-order polynomial fit, which matches best all the values: $\lambda_0/d = \sum_i m_i Re^i$, with $m_0 = 11.8$, $m_1 = -0.129$, $m_2 = 9.74\times10^{-4}$, $m_3 = -3.59\times10^{-6}$ and $m_4 = 5.32\times10^{-9}$. The agreement between (3.3) and the measured values is good.

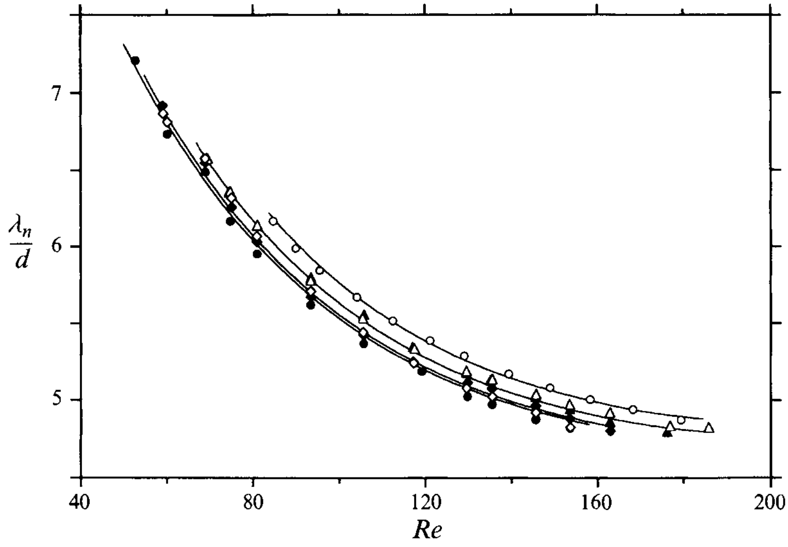

FIGURE 6. Streamwise wake wavelength as function of Reynolds number and shedding mode for the ring with aspect ratio $\pi D/d = 59.0$. Symbols as in figure 3. The lines represent a least-squares fit of the family (3.3) to the measured data.

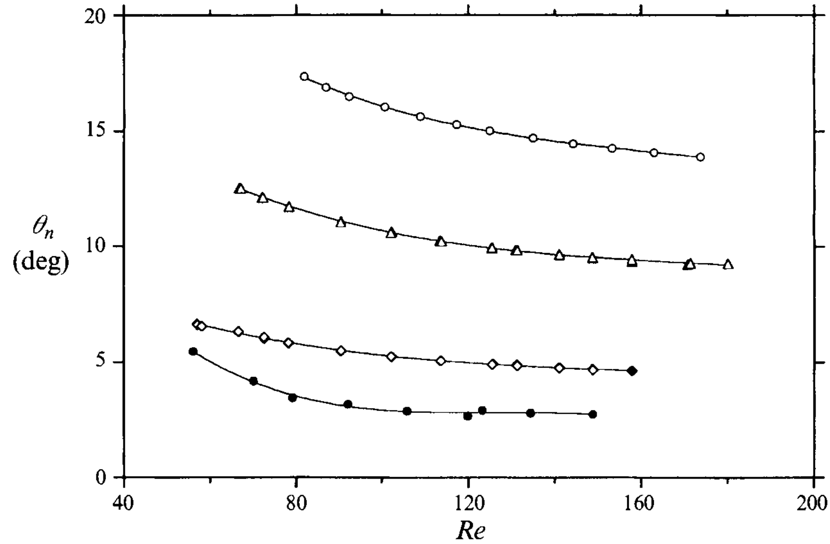

FIGURE 7. Shedding angle in the developed plane of the wake as function of Reynolds number, calculated from the data in figure 6 using (3.2) and (3.4). Symbols as in figure 3.

Figure 7 shows the shedding angles of the different modes as a function of Reynolds number, calculated from (3.2) for the helical modes and using the wavelength data shown in figure 6. For mode 0, because of the inclination of the vortex rings, the mean absolute value of the shedding angle in the developed wake plane was determined from phase measurements as in figure 3 and the formula

$$\theta_0 = \tan^{-1}[\lambda_0(\Delta\Phi_{max} - \Delta\Phi_{min})/\pi^2 D]. \tag{3.4}$$

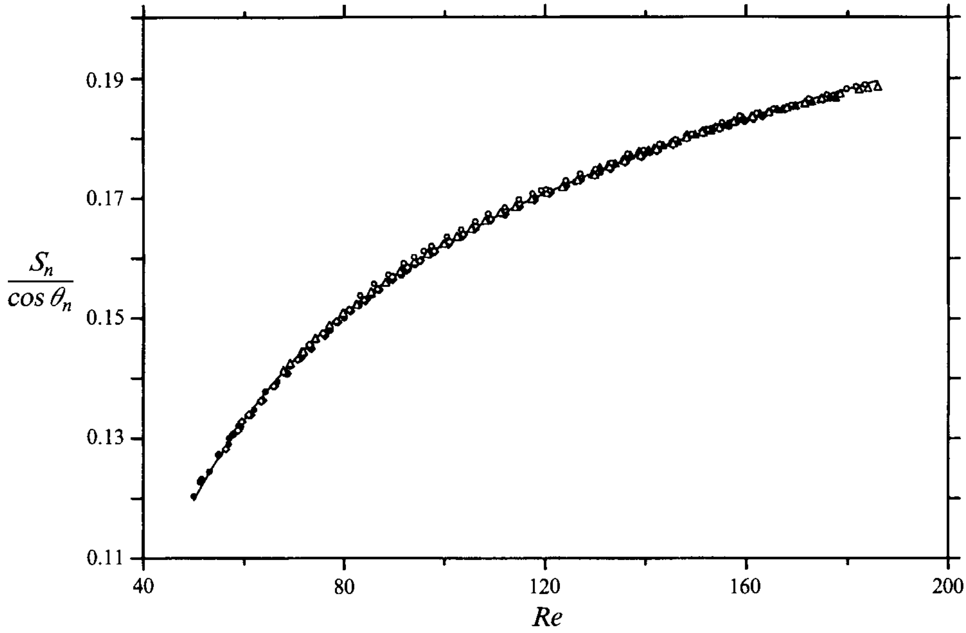

FIGURE 8. The Strouhal curve for parallel shedding behind the ring of aspect ratio $\pi D/d = 59.0$, obtained from the original data in figure 5 using (3.1) and interpolations of the data in figure 7 for θ. Symbols as in figure 3.

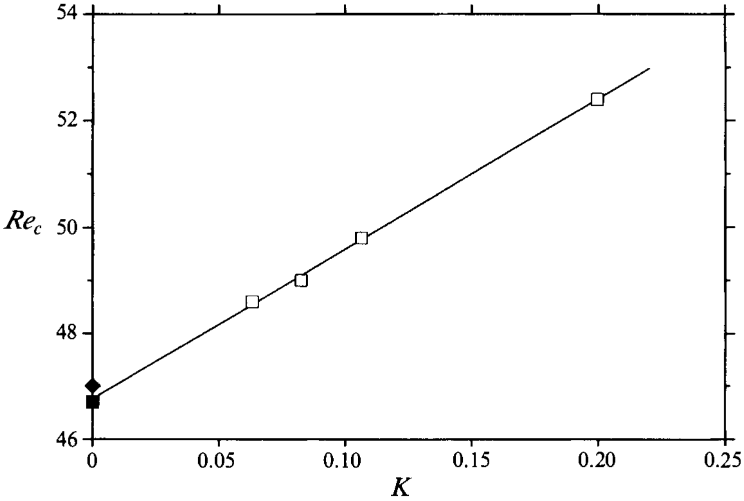

FIGURE 9. Critical Reynolds number for the onset of the Bénard–von Kármán instability as function of the normalized body curvature normal to the flow. Present measurements on rings (□); straight cylinders for $L/d \to \infty$: Mathis *et al.* 1984 and Norberg 1994 (◆); Schumm *et al.* 1994 (■).

The helix angles are roughly proportional to the mode number n in the range of values observed, i.e. between 0° and 18°.

Finally, the data in figures 5 and 7 for S and θ were used to calculate S_0, i.e. the Strouhal number of parallel shedding, from (3.1); the result is shown in figure 8. As in the case of straight cylinders (Williamson 1988*a*) the transformed frequency laws of the

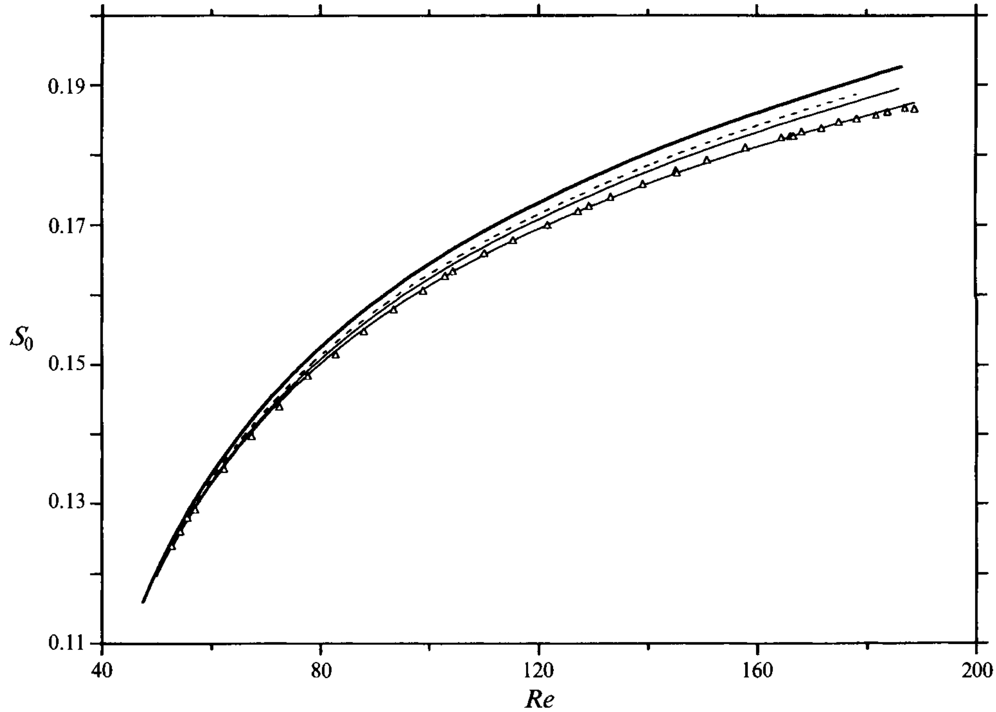

FIGURE 10. Comparison of the Strouhal curves for parallel shedding for rings of different aspect ratios: $\pi D/d = 99.5$ (----), 59.0 (——), and 31.5 (——△——). ——, Straight cylinder.

ring cylinder wake collapse to a single curve, despite the body curvature. This again shows that the effect of the curvature is small; its precise influence is examined in the following section.

3.3. *Curvature effects*

Before returning to the Strouhal curves, the influence of the transverse body curvature on the critical Reynolds number Re_c for the transition from a stationary to an oscillating wake is analysed. The fact that this instability is characterized by a supercritical Hopf bifurcation allows a very accurate determination of the critical Reynolds number from measurements of the oscillation amplitude, as described in more detail in §5.2. In figure 9, Re_c is plotted against the non-dimensional curvature $K = 2d/D$ of the four rings. The curvature tends to increase the critical Reynolds number, and an approximately linear dependence is found. This linear variation can be extrapolated down to zero curvature, yielding $Re_c(K = 0) = 46.8$, which is very close to the values for long straight cylinders found by Mathis *et al.* (1984) and Schumm *et al.* (1994), who both used related methods for the determination of Re_c, and the one announced by Norberg (1994) for a cylinder with a very high aspect ratio ($L/d \approx 2000$).

The procedure described in the last section has been used to determine the Strouhal–Reynolds number relationships for parallel shedding behind the rings. These relationships are very well approximated by the formula

$$S_0 = A/Re + B + C\,Re. \tag{3.5}$$

The values of the coefficients A, B, and C are given in table 1, and three of the four Strouhal curves are plotted in figure 10, where they are compared to the straight

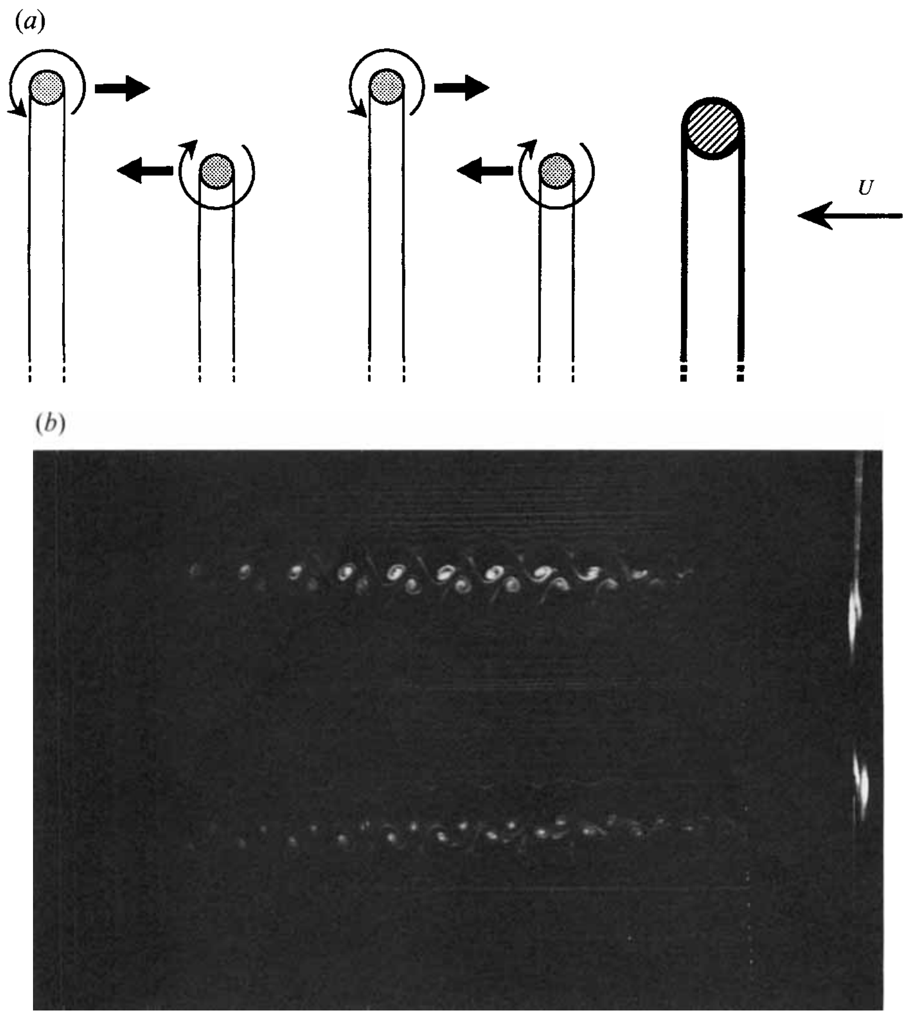

FIGURE 11. The influence of body curvature on the vortex street configuration: schematic representation of the self-induced velocity of the curved vortices (*a*), and a smoke visualization (*b*) of the resulting asymmetry in the longitudinal vortex spacing.

Cylinders	1	2	3
d (mm)	2.01	1.01	1.01
L (mm)	157	120	120
L/d	78	119	119
End configurations	Angled (15°) end plates, ∅40 mm	Angled (12°) end plates, ∅20 mm	End plates, ∅20 mm, and end cylinders, ∅2 mm, length 15 mm

$$S_0 = -3.810/Re + 0.1904 + 1.220 \times 10^{-4} Re$$

TABLE 2. Dimensions, end configurations, and Strouhal curve for the circular cylinders.

circular cylinder result for parallel shedding, given by the bold line. The latter represents the collected data from three cylinders, which are described in more detail in table 2. Figure 10 shows that, at a given Reynolds number, the shedding frequency decreases with growing curvature and that near the instability threshold the differences between the curves seem to vanish.

This decrease of the Strouhal number can be qualitatively understood by the following considerations. It is a well known fact that curved vortices, and in particular vortex rings, move in the surrounding fluid with a *self*-induced velocity perpendicular to the plane of curvature (see e.g. Saffmann 1992). For the vortex configuration in the ring wake, a part of which is shown schematically in figure 11 (*a*) for the case of parallel shedding, this means that the counter-rotating vortices have the tendency to pair, instead of showing a symmetrical spacing. This is actually observed in the experiments (see figure 11*b* and the visualizations of Ehrhardt 1979 and Takamoto 1987). Furthermore, the velocity induced on each vortex by the other vortices of the vortex street is directed in the upstream direction, which is one of the reasons why the vortex convection speed U_c is somewhat less than the free stream velocity. As can be seen from a simple geometrical consideration and the assumption of potential vortices, this velocity induced by the other vortices has a minimum for the symmetrical configuration, for given values of the vortex circulations. This means that any dissymmetric spacing results in a higher induced velocity upstream, i.e. a lower vortex convection speed U_c, and consequently a lower wake frequency. It is also intuitively clear that this effect gets stronger with increasing curvature (higher self-induced velocity) and increasing vortex strength (all induced velocities higher), which makes it plausible why the frequency differences vanish at the threshold.

Nevertheless, no simple expression giving the frequency shift as function of Reynolds number and curvature can be deduced from these ideas, owing to the difficulties in evaluating how close the counter-rotating vortices get to each other and how much the circulations of inner and outer vortices are modified by the curvature, a fact which had been noticed by Roshko (1953) already. Therefore this dependence is here determined from the experiments.

From figure 10 and the fact that curvature effects are small (maximum deviation from the straight cylinder frequency of about 5%) a linear variation in K is assumed in the following form:

$$S_0(Re, K) = S_0(Re, 0) - g(Re)\,K, \tag{3.6}$$

where $g = |\Delta S_0/\Delta K|$. The function g was calculated for all pairs of Strouhal curves among the results for the four rings (figure 12). When discarding the combinations for which the differences in curvature (and therefore frequency) are too small to give reliable results, a linear dependence on Reynolds number emerges for the remaining ones. Since it is desirable to have g independent of K, the following relation is proposed from the results shown in figure 12:

$$g(Re) = a[Re - Re_c(K = 0)]. \tag{3.7}$$

Equations (3.1), (3.6), and (3.7) then yield a global expression for the Strouhal number in the periodic regime of bluff body wakes with circular cross-section:

$$S(Re, K, \theta) = \{S_0(Re, K = 0) - a[Re - Re_c(K = 0)]\,K\}\cos\theta. \tag{3.8}$$

A least-squares fit (bold line in figure 12) gives $a = 2.134 \times 10^{-4}$. With this, the function $S_0(Re, K = 0)$ can now be calculated from the measured sets of data via (3.6) and (3.7). The result is given in figure 13 and it confirms the validity of the assumptions made

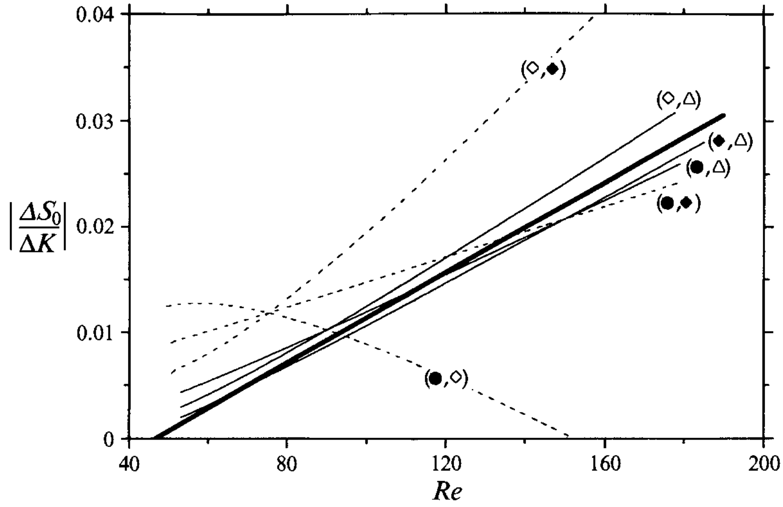

FIGURE 12. The function $g(Re)$ in (3.6), calculated from pairs of the experimentally determined Strouhal curves of four rings of different curvature. Symbols as in figure 14. – – –, $\Delta K < 0.05$, the differences in S and K for these curves are too small to deduce g reliably; ——, $\Delta K > 0.05$; ——, linear fit $\propto [Re - Re_c(K = 0)]$ to the curves with $\Delta K > 0.05$.

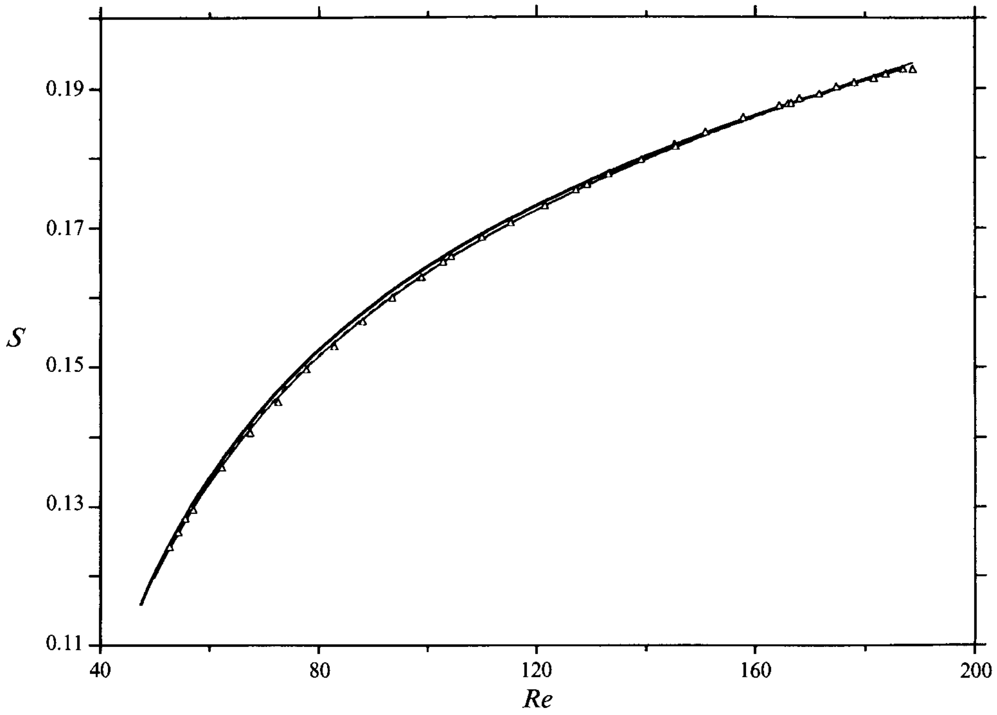

FIGURE 13. Universal Strouhal curve for parallel vortex shedding behind an 'infinite' circular cylinder, obtained by extrapolation of the ring wake results down to $K = 0$ using (3.6) and (3.7), and comparison with the straight cylinder case. Lines and symbols as in figure 10.

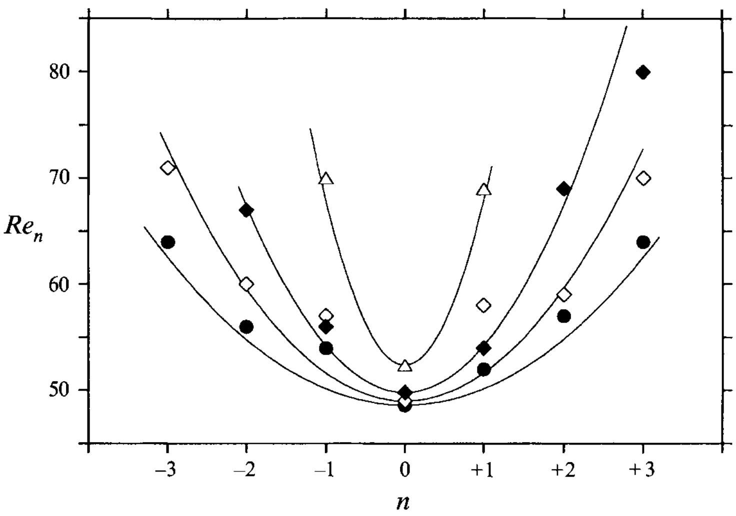

FIGURE 14. Eckhaus stability limits for rings of different aspect ratios. $\pi D/d = 99.5$ (●), 76.2 (◇), 59.0 (◆), and 31.5 (△). The lines represent the predictions of the Ginzburg–Landau model (equation 5.12).

above: the curves obtained for the three rings of figure 10 are practically identical. A least-squares fit of the form (3.5) of all the transformed data gives

$$S_0(Re, K = 0) = -3.669/Re + 0.1861 + 1.432 \times 10^{-4} Re. \tag{3.9}$$

Even if a more theoretical foundation for (3.6) and (3.7) is lacking, the fact that over 500 data points for 23 different combinations (K, n) can be collapsed, via (3.8), onto the single curve (3.9), with an average percentage error of 0.24%, shows that it is nevertheless an excellent approximation. Equation (3.9) was obtained from an extrapolation of the results from experiments on curved bluff bodies without ends (rings) down to zero curvature. It can therfore be considered as an experimentally determined Strouhal curve for parallel vortex shedding behind straight cylinders of infinite length.

A comparison with the present results from experiments on straight cylinders with ends, determined independently from the procedure described in this section, is also made in figure 13. The two curves are practically identical. Equation (3.9) also agrees extremely closely with the 'universal' Strouhal–Reynolds number relationship defined previously for straight cylinders by Williamson (1988*a*) and the parallel shedding data by Norberg (1994). Thus, within experimental uncertainty, the two methods of determining the Strouhal curve of truly two-dimensional vortex shedding, i.e. measurements on straight cylinders with special end configurations (including transformation of oblique shedding data) and the present method of extrapolating ring wake data to zero curvature, give the same result.

3.4. *Secondary instability of the helical shedding modes*

In this section the phenomena associated with the lower stability limit of the helical ring wake modes are described. The stability diagram in figure 4 shows that a given mode with $n \neq 0$ is not stable below a certain Reynolds number Re_n, which is an increasing function of $|n|$. In figure 14 the stability limits of all the modes observed in the wake of four rings are collected. The same tendency is observed in all cases, and it gets stronger with decreasing aspect ratio. In §5.3 it is shown that this

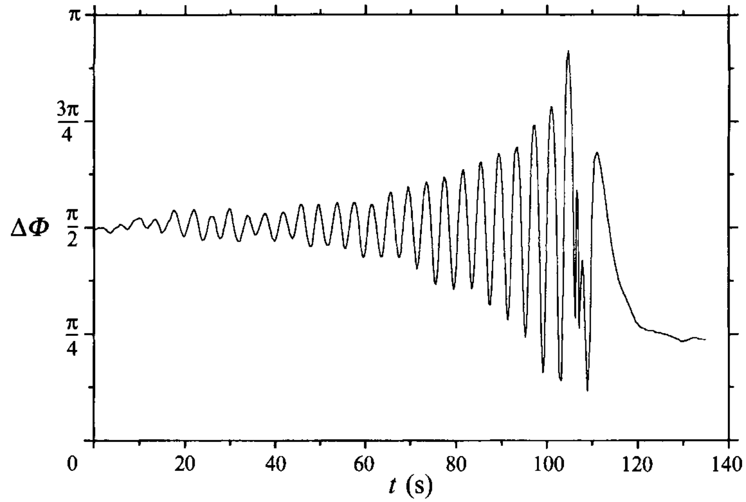

FIGURE 15. Transition from mode -2 to mode 0, after a change in Reynolds number from $Re = 68.1$ to 66.7 at $t = 0$, for the ring with $\pi D/d = 59.0$: time evolution of the difference $\Delta\Phi$ between the phases of the velocity fluctuation at two spanwise positions, chosen to have $\Delta\Phi(t < 0) = \pi/2$ for reasons for signal processing.

really is an effect linked to the aspect ratio (the spanwise confinement) and not to the curvature of the body. It is also shown that Ginzburg–Landau model predicts a relation $(Re_n - Re_c) \propto n^2$, which is plotted as solid lines in figure 14.

When the ring wake is in a helical mode n and the Reynolds number is decreased from above to below the limit Re_n, the initial mode becomes unstable, and a transition to a new, stable mode takes place. This transition happens in a very characteristic way, which was discovered by observing the Lissajous figures of the velocity signals from the two fixed hot wires at different spanwise positions. In the stable domain, these figures are also perfectly stable. When passing the stability limit, the Lissajous begins to oscillate slowly with an amplitude growing in time, until it breaks down in a short moment of chaotic motion before restabilizing in a new shape. This qualitative observation can be quantified by measuring the phase difference between two velocity signals as a function of time. Figure 15 shows a typical record of this phase difference after a step change in Reynolds number across the stability limit. Constant before the change, it begins to oscillate with an amplitude growing approximately exponentially, until the initial mode breaks down. No nonlinear saturation of the phase fluctuation amplitude was observed. The wake then reorganizes itself in a different mode with lower $|n|$, which is still stable at the new Reynolds number, and the phase difference becomes constant again. It is interesting to note the time scales involved in this transition. For the case shown in figure 15, it takes about 2 minutes. With the shedding frequency being close to 15 Hz, this represents almost 2000 vortex shedding cycles. It is also clear that the duration of the free stream velocity transient for the Reynolds number change, which is of the order of 1 s, is completely negligible.

The phase fluctuations $\Delta\Phi$ of figure 15 have the approximate form

$$\Delta\Phi \propto \exp(\alpha_n t) \sin[\omega_n t + \text{const.}], \tag{3.10}$$

where the growth rate α_n and the frequency ω_n of the fluctuations depend on the initial mode n. Both these quantities have been determined for a number of cases from time records as in figure 15. The dependence on Reynolds number of the growth rates, non-

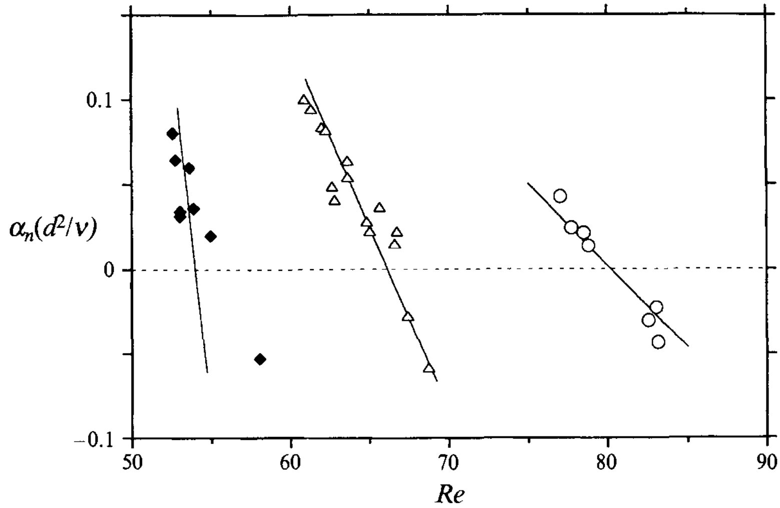

FIGURE 16. Dimensionless growth rate of the Eckhaus instability of the helical vortex patterns, determined from measurements as in figure 15. Symbols as in figure 3. Lines represent the predictions of the Ginzburg–Landau model (equation (5.13)).

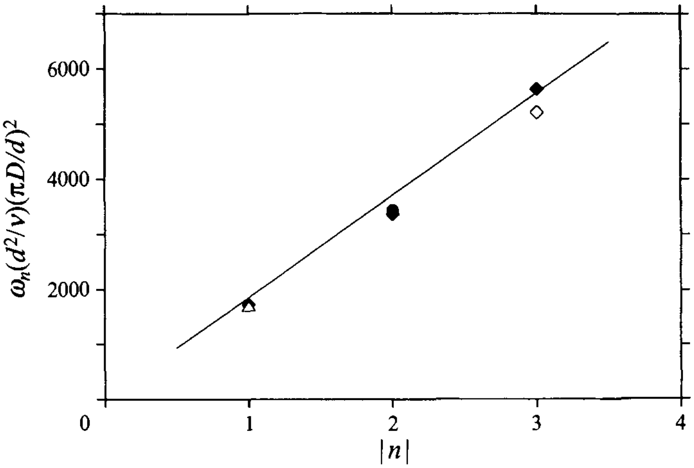

FIGURE 17. Normalized dimensionless frequency of the Eckhaus phase fluctuations. Symbols as in figure 14. The line represents the prediction of the Ginzburg–Landau model (equation (5.14)).

dimensionalized with the viscous diffusion time, for three modes can be seen in figure 16. Within the limits of experimental uncertainty, this dependence is linear, and the α_n are proportional to the threshold deviation $Re-Re_n$. Negative growth rates were found by letting the instability grow with $Re < Re_n$ and by switching to $Re > Re_n$ in time before the initial mode broke down.

Figure 17 gives the non-dimensional phase fluctuation frequency for different rings, multiplied by the square of the aspect ratio, which is motivated in §5.3. This quantity is then proportional to the wake mode number n. In other words, the lower the aspect ratio and the higher the winding number of the initial mode, the higher the frequency of the phase fluctuations associated with this secondary instability. During the transition process the velocity spectra exhibit sideband peaks at the combinations between shedding and phase fluctuation frequencies and the latter are of the same order of magnitude as the differences between the shedding frequencies of the different modes at a given Reynolds number. These observations already suggest a mode interaction as the mechanism responsible for the destabilization of the oblique shedding patterns. This is confirmed in §5.3.

Furthermore, the interpretation, in the framework of the Ginzburg–Landau wake model, of the phenomena described in this section identifies them as a well-known instability in dynamical systems: the modulational or Eckhaus instability of an array of coupled oscillators. Although it has been observed in closed flow systems, and particularly in thin-layer cellular convection (see e.g. Lowe & Gollub 1985; Kramer & Zimmerman 1985; Tuckermann & Barkley 1990), it has never been identified experimentally for open flows.

4. Experimental results. II. The transition range

The phenomena described in this section occur at Reynolds numbers just above the periodic regime in the approximate interval $150 < Re < 350$.

For circular cylinders the periodic vortex street becomes unstable at a Reynolds number Re_t of the order of 180. This value is only indicative. A surprisingly large range of quoted transition Reynolds numbers exists in the literature. Examples are $Re_t = 150$ (Roshko 1953; Tritton 1959), $Re_t = 165$ (Norberg 1994), $Re_t = 178$ (Williamson 1989), and $Re_t = 205$ (Williamson 1995). The explanations proposed for this discrepancy include a varying free stream turbulence level (Bloor 1964), a difference between parallel and oblique vortex shedding (Hammache & Gharib 1989) and the influence of the cylinder end configuration (Williamson 1995).

Figure 18 shows the values of Re_t as a function of the wake mode for the different rings. In this configuration, the 'end' conditions are strictly the same for all the measurements, and the turbulence level can also be considered as being constant. For a given ring, a dissymmetry between left- and right-turning helical modes can be seen, and no clear evolution of, for example, the minimal transition Reynolds number with the ring aspect ratio can be deduced. This is probably due to the perturbations induced by the support wires and the sensitivity of the transition point to experimental conditions, as mentioned above. Nevertheless, a tendency for the higher-order helix modes to remain stable longer than the lower-order or vortex ring modes is observed, a tendency which seems to increase with curvature. The results in figure 18 for a configuration without end effects thus suggest that oblique shedding is more stable than parallel shedding. However, with the known sensitivity of the transition even to small perturbations, it cannot be ruled out that this behaviour is caused by the body curvature.

When the Reynolds number is increased across the transition range, i.e. from Re_t to about 350, different ring wake behaviours are observed. Just above the transition point the velocity fluctuations are no longer periodic, as for lower Re (figure 19*a*), but rather chaotic (figure 19*b*), showing large fluctuations in amplitude and frequency (see the spectra in figure 20). The frequent appearance of amplitude 'holes' (arrow in figure 19*b*), which indicate the passage of vortex dislocations (Eisenlohr & Eckelmann 1989; Williamson 1989) is also observed in this Reynolds number region. Williamson (1992) investigated in detail the transition in the wake of straight cylinders with ends. With reference to his results, which show a very similar behaviour, the kind of vortex shedding described above is named mode A.

For higher Reynolds numbers the wake fluctuations become more periodic again, i.e. the dominating frequency is much better defined, and few dislocations occur. The

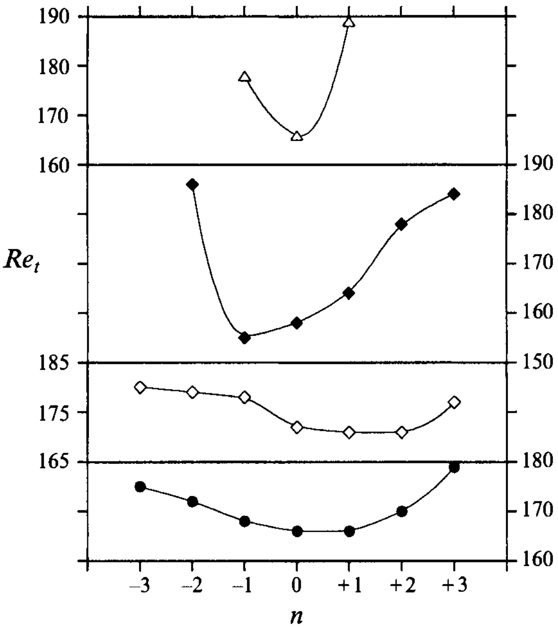

FIGURE 18. Transition Reynolds number, i.e. upper stability limit, of the periodic shedding modes for four rings. Symbols as in figure 14, curvature increases from bottom to top.

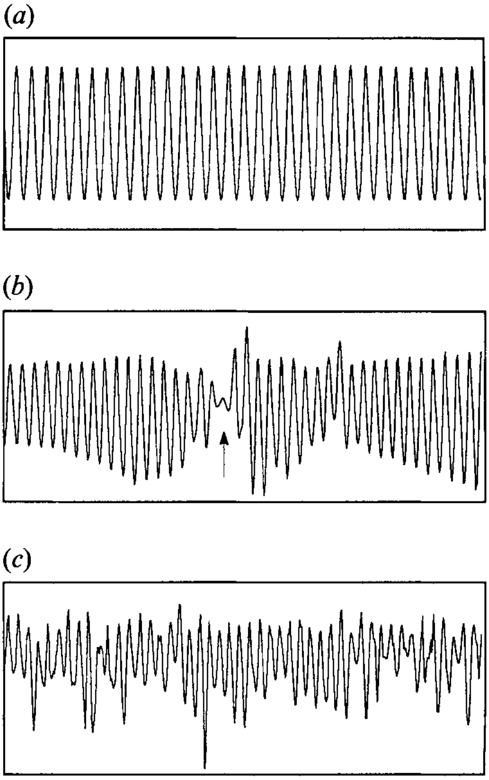

FIGURE 19. Time traces of the velocity fluctuations for the different transition modes, measured at $x = 7d$ and $y = -2d$. Ring of aspect ratio $\pi D/d = 76.2$. (*a*) $Re = 152$ (periodic); (*b*) $Re = 194$ (type A); (*c*) $Re = 412$ (type B).

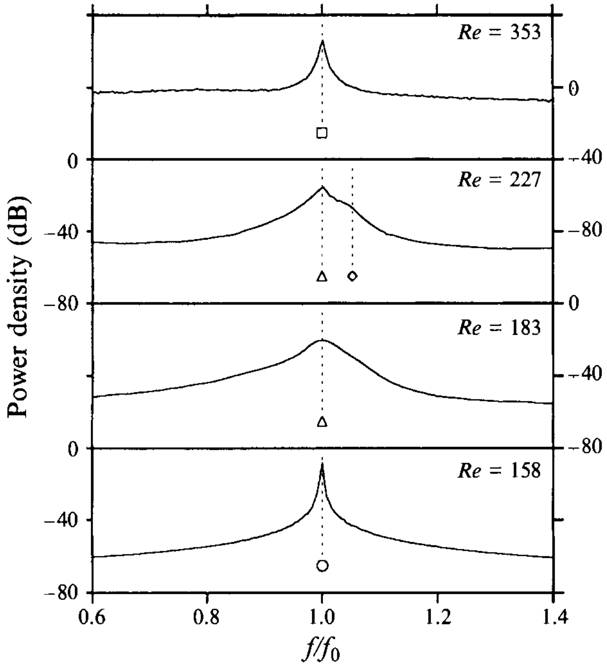

FIGURE 20. Spectra (long-time averages) of the velocity fluctuations. Ring of aspect ratio $\pi D/d = 59.0$. ○, Periodic mode: △, mode A; ◇, mode A*; □, mode B.

seemingly more irregular time trace of the velocity fluctuations shown in figure 19(*c*) is due to small-scale three-dimensional perturbations in the form of counter-rotating streamwise vortices, 'superimposed' on the primary, more coherent vortex shedding. This corresponds to Williamson's mode B.

The two transition modes A and B are well characterized by their long-time velocity spectra, shown in figure 20 for the ring of aspect ratio 59.0. Whereas in the periodic regime one sharp peak (plus harmonics) is visible ($Re = 158$), the spectrum of mode A ($Re = 183$) shows a large band around a centre frequency f_0 which is not very well defined. The width of the peak is considerably smaller in mode B ($Re = 353$), but the 'background' perturbation level, which manifests itself as a 'white noise' in the spectrum, continues to increase with Reynolds number. For intermediate *Re* a second frequency can be identified in the velocity spectra (figure 20, $Re = 227$) by a hump on the primary peak. It is visible in the range $200 < Re < 300$ approximately, but its intensity never exceeds that at f_0.

The domains of these modes and the transitions between them are best illustrated by a plot of the Strouhal numbers associated with the different frequencies from the velocity spectra versus Reynolds number (figure 21*a*). The transitions from the periodic modes to mode A are characterized by a discontinuity in the Strouhal curve, and the corresponding branches overlap in a certain interval. The wake behaviour in this zone is quite complicated. It is shown in figure 18 that the different periodic modes have different transition Reynolds numbers Re_t. When increasing the Reynolds number in a periodic mode across its transition point, the wake either changes directly to another stable periodic mode or it switches abruptly to mode A, depending on the Reynolds number. In the latter case, and if there are other periodic modes which are still stable at this new *Re*, the wake returns to one of them after a random time interval and then stays in that mode indefinitely (the time spent in mode A can be extremely

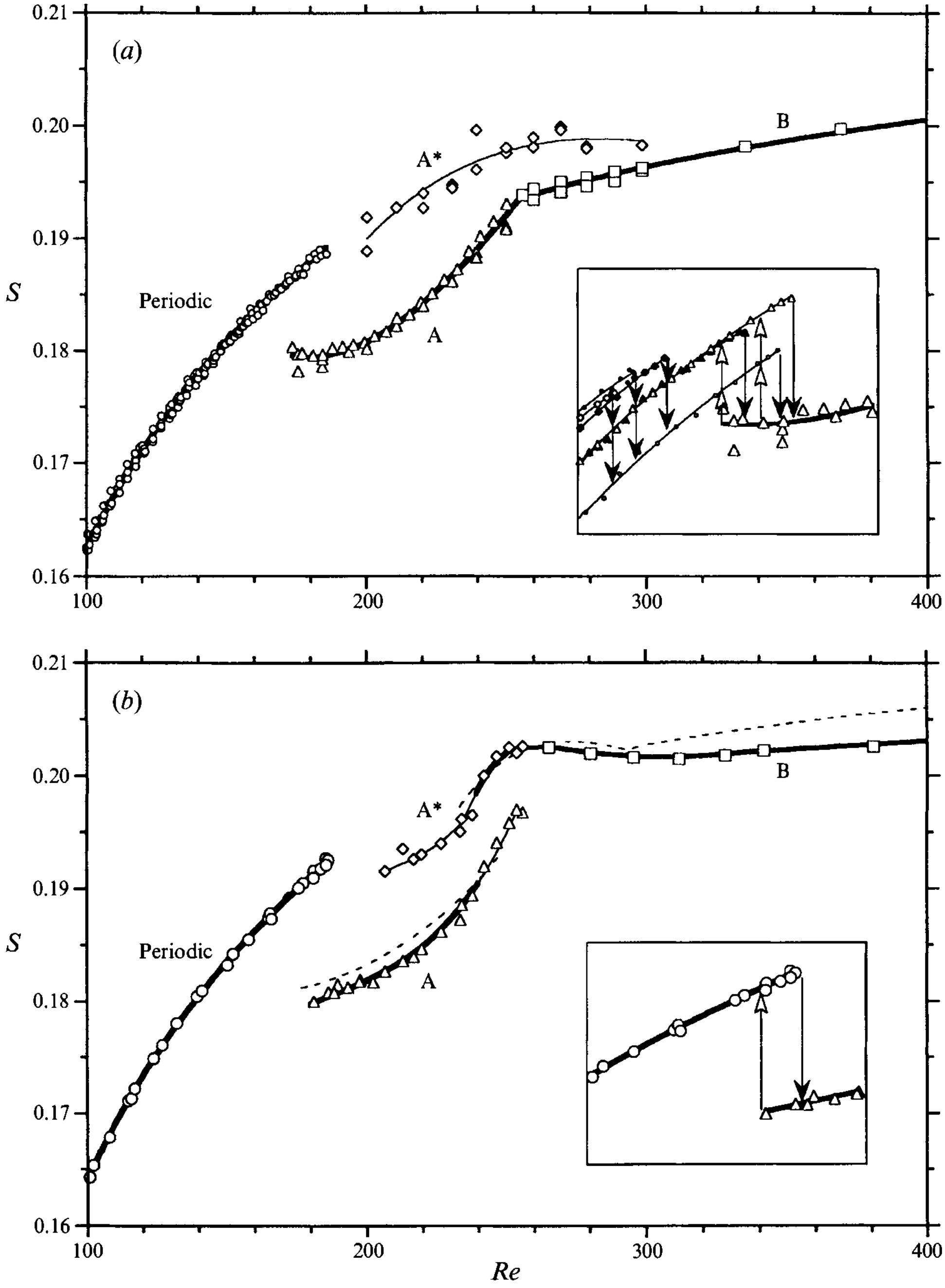

FIGURE 21. Strouhal number in the transition range: (*a*) ring, aspect ratio $\pi D/d = 59.0$, only the parallel shedding curve is shown in the laminar mode; (*b*) straight cylinder, aspect ratio $L/d = 78$. ——, dominating frequencies; ----, Williamson (1991). Symbols as in figures 3 and 20.

long, of the order of tens of thousands of shedding cycles). This is true for most of the lower part of the overlap, even when it is reached from the higher side. There is however a small interval at the upper end of the overlap region where this has never been observed, i.e. there exists a slight hysteresis at this point. When the Reynolds

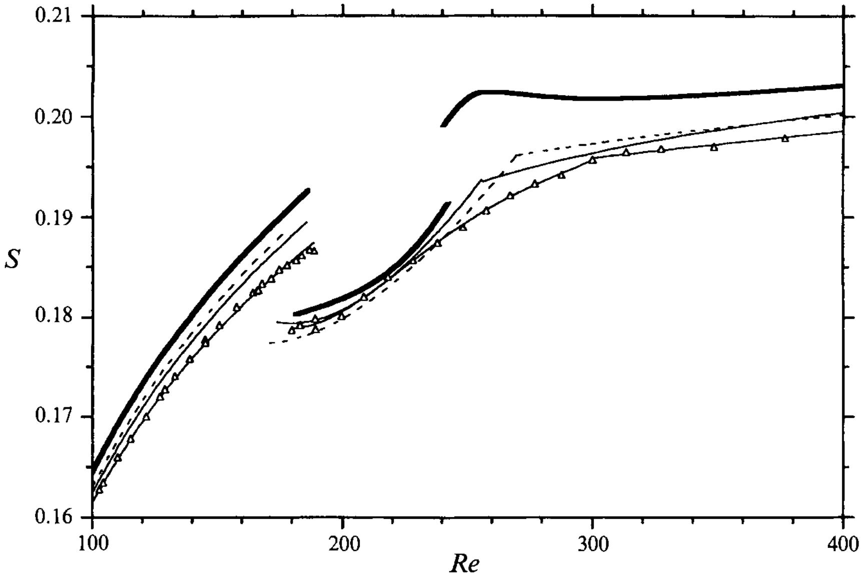

FIGURE 22. Comparison of the Strouhal curves of different rings and a cylinder in the transition range. Only the curves corresponding to the maximum in the spectrum are plotted. Lines as in figure 10.

number is decreased from a higher value into the overlap region, the wake returns to a periodic mode only at some distance from the highest Re_t.

During the passage from mode A to mode B, the Strouhal–Reynolds number relationship is continuous, but a pronounced discontinuity in its slope occurs at $Re \approx 260$. The evolution of the velocity spectra is also continuous and not marked by a sudden jump between modes as in the transition between the periodic modes and mode A. The branch associated with the weak third transition mode (A*) seems to align with the parallel periodic curve, which may be a sign that this intermittent mode is a remainder from the periodic regime.

Figure 21 (*b*) shows the corresponding Strouhal data for the straight circular cylinder with ends. The basic mode characteristics are the same as described above for the ring, but there are important differences in the transition between the modes. Concerning the first transition, it is also hysteretic, but over the entire overlap region. This means that mode transitions only occur at the ends of the Strouhal branches. Furthermore, the transition between modes A and B is characterized by a second discontinuity. After the appearance of mode A*, its energy increases until, at $Re \approx 240$, it exceeds that contained in mode A. The latter disappears completely at $Re \approx 260$. The subsequent passage from A* to B is again continuous in frequency.

In figure 21 (*b*) the results for the cylinder are compared to the data of Williamson (1988*b*), who discovered the two discontinuities, the hysteresis, and the shift of energy in the velocity spectra during the A–B transition (no other work concerning these points can be found in the literature so far). His visualizations also revealed the spatial structure of the modes A and B (Williamson 1991), and the description given above for the ring wake are, to a certain point, inspired by this work.

Curvature effects in the transition region are illustrated in figure 22, where the Strouhal curves of three rings are compared to the straight cylinder result. The shedding frequencies are generally lower for the rings, as in the periodic regime, but no clear dependence could be determined. However, the effect of curvature seems to be smaller in mode A. The behaviour at the transitions between the modes, described above for one particular ring, was principally the same for all the rings, i.e. up to the highest aspect ratios, as can be seen from the similar shape of the Strouhal curves in figure 22. It is believed that the differences between rings and cylinders in this flow regime are mainly due to the different end conditions, and that the intrinsic features of the wake of truly two-dimensional bodies are probably better represented by the ring wake results. This is further supported by a preliminary result of the present study involving a ring which had the same dimensions as the present one with aspect ratio 99.5, but which presented a local defect (*d* 2% lower). This can be considered as some kind of perturbing boundary condition. In the transition range, the wake behind this ring behaved exactly like the wake of a straight circular cylinder with ends, as shown in figure 21 (*b*).

The transition modes and especially their spatial structure can further be chartacterized quantitatively by the study of the spanwise correlation of the vortex shedding. The spanwise correlation coefficient C of the wake velocity fluctuations v at given downstream and transverse positions x and y is defined by

$$C(\Delta z) = \max_{-\frac{1}{2f_0}<\tau<\frac{1}{2f_0}} \frac{|\overline{v(z,t)\,v(z+\Delta z,t+\tau)}|}{[\overline{v^2(z,t)}\,\overline{v^2(z+\Delta z,t)}]^{1/2}}, \tag{4.1}$$

where the overbar denotes the average over time t. The maximum over one principal shedding period is taken in order to account for a possible mean phase shift due to a local mean inclination of the vortex lines.

This coefficient was measured for the ring with aspect ratio 59.0, and its evolution in the transition range is shown in figure 23 (*a*) for a spanwise separation $\Delta z = \pi D/4$, i.e. one quarter of the ring perimeter. In the periodic regime, the spanwise correlation is perfect, except very close to the transition point. It seems as if the transition announces itself by a very subtle perturbation of the vortex shedding, barely visible on the Lissajous figures. In mode A the correlation falls to very low values and reaches a minimum at $Re = 260$, which coincides with the discontinuity in the slope of the Strouhal curve in figure 21 (*a*). This is also the Reynolds number of a sharp maximum in the base suction coefficient, which has been measured in straight cylinder wakes by Williamson & Roshko (1990) and Norberg (1994). Also for straight cylinders, Gerrard (1978) found from visualizations in the transition range that what he called 'fingers of dye' occurred most frequently at $Re \approx 250$. These vortex loops have a strong decorrelating effect and the minimum of the spanwise correlation in figure 23 (*a*) may therefore be related to this observation.

For the Reynolds number of this minimum, the entire correlation function $C(\Delta z)$ is given in figure 23 (*b*). It shows an approximately exponential decay, but a discontinuity in the slope appears repeatably at a spanwise separation of about three body diameters. This may be related to the observation of Williamson (1992) that the average spanwise wavelength of the vortex deformation in mode A, determined from visualizations, has approximately the same value. When the correlation length ξ is defined as the area under the curve $C(\Delta z)$, one has for the result in figure 23 (*b*)

$$\xi = \int_0^{\pi D/2} C(\Delta z)\,\mathrm{d}\Delta z \approx 6.3d, \tag{4.2}$$

which is about one tenth of the ring perimeter.

Above $Re = 260$ the spanwise correlation increases rapidly until it reaches a maximum of 0.7 near $Re = 350$, from whereon it slowly decreases again. This

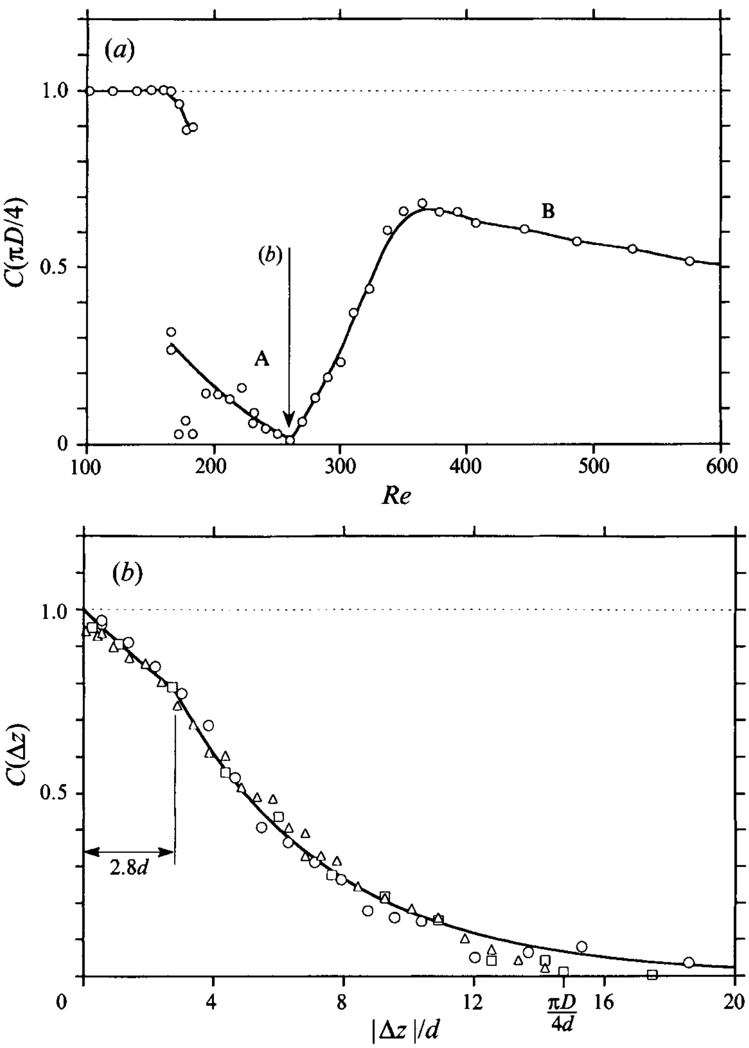

FIGURE 23. Correlation coefficient (see (4.1)) of the velocity fluctuations at two spanwise positions, z and $z+\Delta z$, for the ring with $\pi D/d = 59.0$: (*a*) as a function of *Re*, $\Delta z = \pi D/4$, i.e. one quarter of the perimeter; (*b*) as a function of Δz at $Re = 260$, i.e. at the minimum of the curve in (*a*). In (*b*), the symbols stand for different values of z and lines are exponential fits.

illustrates well the transition to a relatively coherent vortex shedding in mode B and the subsequent slow increase in the small-scale perturbations in the form of streamwise vortices.

The beginning of the transition to turbulence in the separated shear layers through a Kelvin–Helmholtz-type instability is generally found to occur only at $Re = 1000$ and thus has no influence on the phenomena described in this section.

5. The Ginzburg–Landau model. I. The periodic regime

In the two preceding sections a number of experimental results concerning bluff body wakes with particularly clean 'boundary' conditions have been presented. In this and the following section it is shown that a surprisingly large part of the observed phenomena can be understood using a simple dynamical model. This is all the more interesting and useful as exact or approximate analytical approaches for the vortex shedding and transition regime either do not exist or are very limited, and the insight gained by numerical simulations is not always obvious for this apparently complicated flow problem. The problem of deriving the Ginzburg–Landau equation, used to represent bluff body wakes, from the fundamental hydrodynamic equations governing this flow seems to be quite a difficult one, and no conclusive result can be found in the literature so far. This question will not be answered in this paper either, so that, for the moment, the Ginzburg–Landau equation keeps its status of a *model* equation, with the most striking argument for its validity being the number of experimental facts that it can account for.

5.1. *The Ginzburg–Landau equation and its solutions*

Mathis *et al.* (1984) and Provansal *et al.* (1987) showed that a two-dimensional cylinder wake could be modelled by a (zero-dimensional) nonlinear Stuart–Landau oscillator. In the Ginzburg–Landau (GL) model three-dimensional effects are taken into account by considering a diffusively coupled one-dimensional chain of these oscillators, distributed along the spanwise direction of the body. This continuous chain of oscillators represents the near-wake formation region as a whole, i.e. it reduces the three-dimensional physical problem to a one-dimensional one. The point is that the dynamical features of the two turn out to be very similar.

The equation of motion for this system is the one-dimensional complex Ginzburg–Landau equation:

$$\frac{\partial A}{\partial t} = \sigma(1+\mathrm{i}c_0)A + \mu(1+\mathrm{i}c_1)\frac{\partial^2 A}{\partial z^2} - l(1+\mathrm{i}c_2)|A|^2 A. \tag{5.1}$$

The real part of the complex amplitude A is proportional to the velocity fluctuations measured in the wake, and σ, μ, l, c_0, c_1, and c_2 are the (real) model parameters, which have to be determined from experiments. Equation (5.1) contains terms for a linear amplification, a diffusive coupling along the spanwise coordinate z, and a nonlinear saturation.

The parameters used here to model the ring wake are the following:

$$\sigma = k\frac{\nu}{d^2}(Re-Re_c), \quad \mu = 10\nu, \tag{5.2a, b}$$

$$l\nu = O(10^{-1}) \text{ in the near wake}, \quad c_0 = \frac{2\pi}{k}\frac{Ro_0}{Re-Re_c}+c_2, \tag{5.2c, d}$$

$$c_1 = -0.65, \quad c_2 = -3.0. \tag{5.2e, f}$$

The linear growth rate σ (with $k = 0.2$) and the value of c_2 are known from circular cylinder studies (Provansal *et al.* 1987; Albarède & Monkewitz 1992; Sreenivasan *et al.* 1986; Schumm *et al.* 1994). The value for the diffusive coupling constant μ was found from the exploitation of the present ring wake results (see §5.2 and Leweke & Provansal 1994*b*). Albarède & Monkewitz (1992) announced a value three times higher for straight cylinder wakes with end effects, but this is believed to be due to a difficulty in the interpretation of the effective cylinder length to be used in the GL model. This point is discussed further by Albarède & Provansal (1995). The nonlinear coefficient $l > 0$ is linked to the oscillation amplitude (see (5.4*a*) below) and therefore varies in

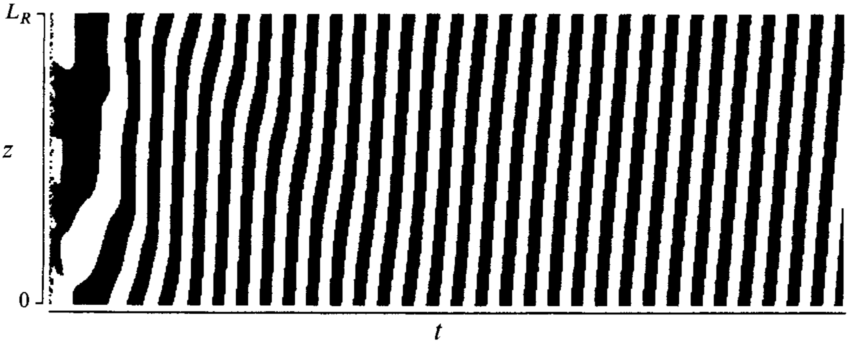

FIGURE 24. Spatio-temporal plot of the real part of the GL amplitude A (positive values in black) showing the development of a helical pattern ($n = 1$) from low-amplitude random noise. Numerical simulation with $c_1 = -0.65, c_2 = -3.0$, and the dimensionless domain length $L_R = 25$ (see A 2b), which corresponds to a ring with $\pi D/d = 59$ at $Re = 59$.

space. It is, however, independent of the Reynolds number. In the expression for c_0 (see next section), $Ro_0 = f_0 d^2/\nu = S_0 Re$ is the Roshko number for parallel vortex shedding. The value for c_1 was found to match best all the experimental data, and it is compatible with the results of Albarède & Monkewitz (1992). The relations (5.2) were found to be valid for $Re_c < Re < 100$ approximately, which is a surprisingly large interval for a model which was *a priori* considered as a development around the threshold Re_c.

In an infinite domain, and for positive values of σ, (5.1) has periodic plane wave solutions

$$A_Q = M_Q \exp[\mathrm{i}(\Omega_Q t + Qz)], \tag{5.3}$$

where the real amplitude M_Q and the frequency Ω_Q are given by

$$M_Q^2 = (\sigma - \mu Q^2)/l, \tag{5.4a}$$

$$\Omega_Q = \sigma(c_0 - c_2) - \mu(c_1 - c_2) Q^2. \tag{5.4b}$$

They both depend on the spanwise wavenumber Q. The cases $Q = 0$ and $Q \neq 0$ correspond to parallel and oblique vortex shedding, respectively. Because of the periodic boundary conditions which apply to the ring geometry, i.e. $A(z = \pi D, t) = A(z = 0, t)$, Q can only take the discrete values discussed in §3.1: $Q = Q_n = 2n/D$ ($n = 0, 1, 2, 3$). It may be emphasized at this point that the periodic boundary conditions are incorporated in the model without problem. For the modelling of wakes behind straight cylinders with ends, the boundary condition $A = 0$ was chosen (Albarède *et al.* 1990) to express the fact that the oscillation has to vanish at the spanwise boundaries. This is only a poor representation of the complicated phenomena in this region, which made the quantitative comparison with experimental data quite difficult (see e.g. Albarède & Provansal 1995). In the present application of the GL model to ring wakes, curvature effects are neglected but, as shown in §3.3, they are only responsible for small corrections and do not notably modify the dynamical wake behaviour.

Figure 24 shows the result of a numerical simulation of (5.1) with periodic boundary conditions in the form of a spatio-temporal plot (a description of the algorithm used for these calculations can be found in Albarède 1991). Starting from random noise, a helical mode with $n = 1$ develops. Knowing that the downstream part of bluff body wakes is mainly made up of convected structures created in the near wake, the transformation $t = -x/U_c$ allows us to consider this plot as a visualization of the

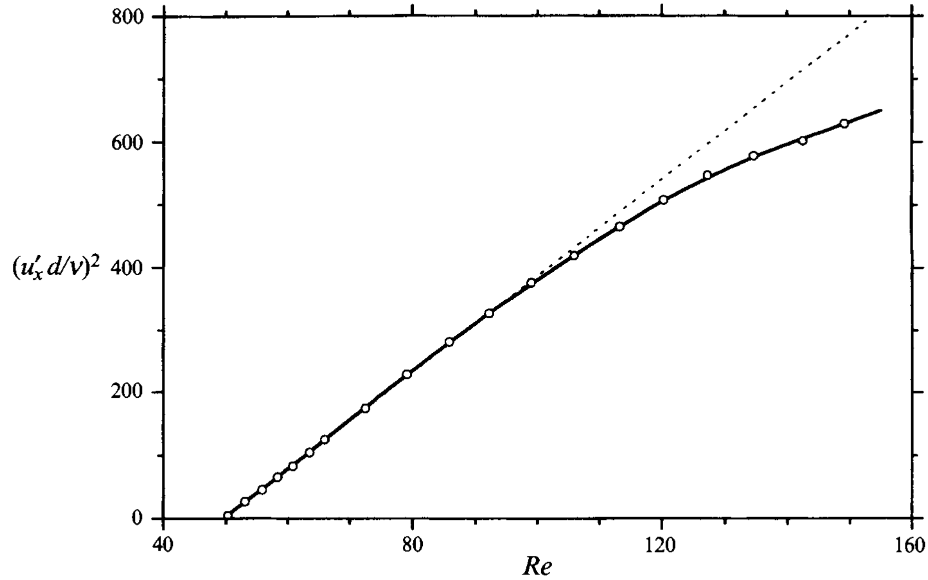

FIGURE 25. Square of the amplitude of the streamwise velocity fluctuation measured at $x/d = 7$ and $y/d = -2$. Ring aspect ratio $\pi D/d = 59.0$, shedding mode $n = 0$.

wake, with the body on the right side and flow from right to left. This is not true in all situations, as will be seen in §6 in the case of dislocations. In experiments these structures show a significant downstream evolution, which is not modelled by the present spanwise GL equation.

5.2. *Amplitudes and frequencies*

Equations (5.3) and (5.2*a*), together with the expression for the discrete spanwise wavenumbers Q_n lead to the following relations concerning the amplitude of the velocity oscillations:

$$(M_0 d/\nu)^2 \propto (Re - Re_c), \tag{5.5}$$

$$\frac{M_n^2}{M_0^2} = 1 - \frac{\mu/\nu}{k(Re-Re_c)} \frac{4\pi^2}{(\pi D/d)^2} n^2. \tag{5.6}$$

Here and in the following, the notations $M_n \equiv M_{Q_n}, \ldots$ etc. are used. Figure 25 shows the square of fluctuation amplitude u'_x of the streamwise velocity component measured at $x = 7d$ and $y = -2d$ in the wake of the $\pi D/d = 59.0$ ring. Relation (5.5) is very closely verified up to $Re = 100$ For higher values the beginning of some kind of saturation is visible. From the point of view of the model it is not clear if this is due to a variation of l or if (5.2*a*) is no longer valid at high Reynolds numbers. Another reason may be that, according to the theoretical analysis of wake flows in terms of global oscillation modes (Goujon-Durand, Jenffer & Wesfreid 1994), the linear behaviour in (5.3) should not necessarily be observed for amplitudes measured at the same point in the wake for all Re, but rather for a 'norm' of the oscillating flow, given for example by the maximum of the amplitude fluctuation.

The linear u'^2_x–Re relationship near the threshold allows a very accurate and unambiguous determination of the critical Reynolds number Re_c of the Bénard–von Kármán instability by extrapolation to zero amplitude. In the 'older' literature, the reported values of Re_c, often deduced from flow visualizations, were sometimes

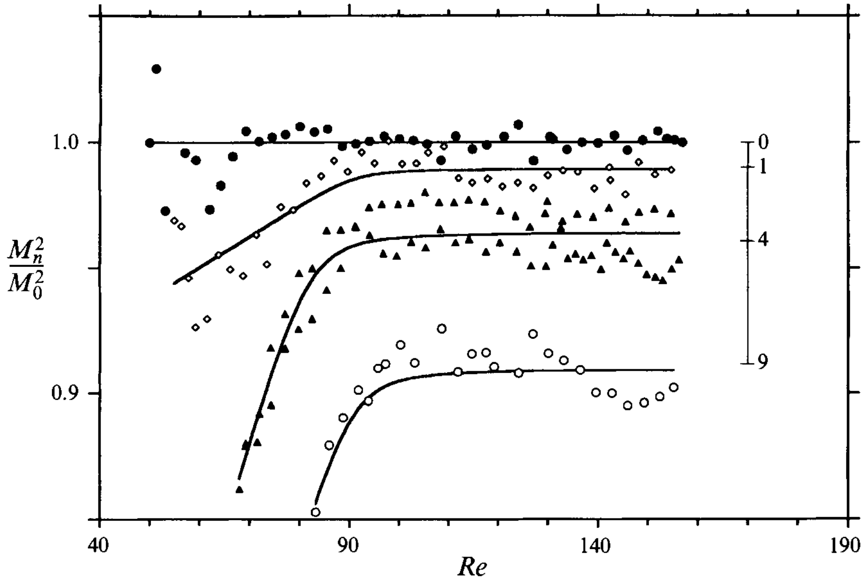

FIGURE 26. Relative fluctuation energy as function of periodic shedding mode and Reynolds number. Ring with $\pi D/d = 59.0$. $|n| = 0$ (●), 1 (◇), 2 (▲), and 3 (○).

significantly lower (see e.g. Gerrard 1978 or the review by Coutanceau & Defaye 1991), probably because of a convective instability developing downstream. At present, values of Re_c around 47 are generally recognized for circular cylinders (see figure 13).

A test of (5.6) is shown in figure 26. The measured oscillation energies of the different modes were divided by a smooth fit of the parallel shedding values. Despite the scatter of the data, a distinct change is visible at $Re \approx 100$. Above this value the relative differences in the mode amplitudes are almost constant and the dependence on n^2, predicted by (5.6), seems to be verified. The results in figure 26 lead to the value for the diffusive coefficient given in (5.2*b*) for $Re < 100$ (Leweke & Provansal 1994*b*).

The origin of the differences between the ranges below and above $Re = 100$, observed in figures 25 and 26, is not clear. The same Reynolds number is sometimes cited as the end of the range where diffusion of vorticity plays the primary role in the vortex formation and the beginning of a regime where vorticity convection becomes dominant (Gerrard 1978; Coutanceau & Defaye 1991). With the Strouhal curves showing no signs of a change in flow behaviour, the result in figure 26 remains the only quantitative support for this idea.

The frequencies of the velocity fluctuations are now known very accurately in the laminar regime and the 'cosθ law' (3.1) has been shown to be valid for straight cylinders and also rings, as described in §3.2. It is therefore necessary to relate the Ginzburg–Landau model to (3.1). For this it is more convenient to use the Roshko number $Ro = fd^2/\nu = S\,Re$, for which the same $\cos\theta$ law also holds. Two relations for the frequencies can be derived from (5.2*a*) and (5.4*b*):

$$Ro_0 \frac{\nu}{d^2} = f_0 = \frac{1}{2\pi}\sigma(c_0 - c_2), \tag{5.7}$$

$$Ro = Ro_0 - \frac{\mu}{\nu}(c_1 - c_2)\frac{(Qd)^2}{2\pi}. \tag{5.8}$$

The subscript 0 denotes parallel shedding (except in c_0). Equation (5.7) immediately leads to the expression (5.2*d*) for c_0. The spanwise wavenumber Q is related to the shedding angle θ via the streamwise wavelength λ of the vortex street: $Q = (2\pi/\lambda_0)\sin\theta$ (Albarède 1991). For (5.8) to be identical with the relation $Ro = Ro_0 \cos\theta$, the following condition has to be fulfilled:

$$\frac{\mu}{\nu}(c_1 - c_2) = \frac{1}{4\pi}\left(\frac{\lambda_0}{d}\right)^2 Ro_0 \left[\frac{2}{1+\cos\theta}\right] \approx \frac{1}{4\pi}\left(\frac{\lambda_0}{d}\right)^2 Ro_0. \tag{5.9}$$

The last approximation is justified because the maximum observed values of θ lie around 20°. The combination of parameters on the left-hand side of (5.9) has been determined from frequency measurements in the wake of a ring using (5.8) (Leweke & Provansal 1994*b*). A comparison with the right-hand side of (5.9), calculated with the straight cylinder data of Williamson (1989) for λ_0 and Ro_0, shows a good agreement, considering that the results come from completely different experiments.

The $\cos\theta$ law seems to be more straightforward than the relation (5.8) from the Ginzburg–Landau model, involving a number of *a priori* unknown parameters with a complicated Reynolds number dependence, and the stability arguments and geometrical considerations invoked by Williamson (1989) and, above all, the excellent agreement with experiments leave little doubt about its validity, even if a rigorous theoretical demonstration is still lacking. However, the Ginzburg–Landau model, itself being purely phenomenological, is no less capable of accounting for the observed dependence of frequency on shedding angle (or, better, spanwise wavenumber), and it can describe a great number of other dynamical features, as shown throughout this section.

5.3. *The Eckhaus instability*

The plane wave solutions (5.3) of the Ginzburg–Landau equation (5.1) can become unstable under certain circumstances. In the present one-dimensional complex case, two major instabilities can occur. One is linked to a change in the parameters c_1 and c_2; it is treated in §6. The other one can occur at constant values of these parameters and depends on the spanwise wavenumber Q of the plane waves: the modulational or Eckhaus instability. The instability mechanism is a resonant amplification of sideband disturbances by nonlinear interaction with the initial mode. A very good account on this is given by Stuart & DiPrima (1978).

For the present case of the shedding instability in the ring wakes shown in §3.4, the analytic treatment of Kuramoto (1984) and Janiaud *et al.* (1992) is followed. Perturbed plane wave solutions (5.3) with discrete wavenumbers of the form

$$A(t,z) = M_n[1+a(t,z)]\exp\{\mathrm{i}[\Omega_n t + Q_n z + \phi(t,z)]\} \tag{5.10}$$

are considered and solutions of the linearized equations for the amplitude and phase perturbations a and ϕ are sought in the form

$$a(t,z) = a_0 \exp(\Lambda_n t + \mathrm{i}qz), \quad \phi(t,z) = \phi_0 \exp(\Lambda_n t + \mathrm{i}qz), \tag{5.11}$$

where q is the spanwise wavenumber and $\Lambda_n = \alpha_n + \mathrm{i}\omega_n$ the complex growth rate of the perturbations (α_n is the real amplification rate, ω_n the frequency of the fluctuations). Details of the calculations are given in the Appendix. The main result is that oblique shedding becomes unstable for wavenumbers (i.e. shedding angles) above a limiting value which is an increasing function of Reynolds number, which means that a mode with a given Q_n becomes unstable below a limiting Reynolds number Re_n. When passing this limit, perturbations with wavenumbers q close (but not equal) to zero are

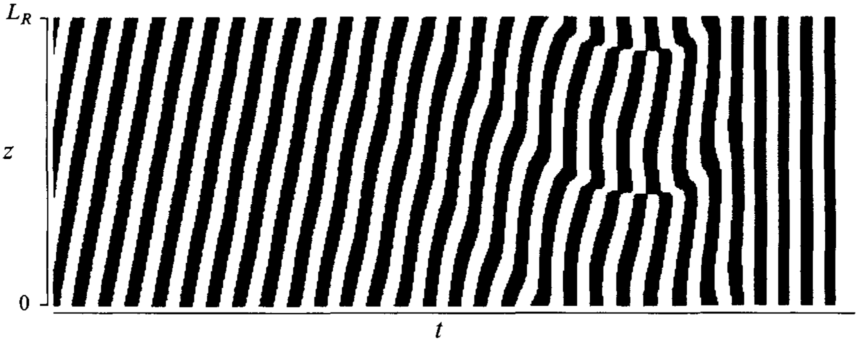

FIGURE 27. Numerical simulation of the Eckhaus instability of mode $n = 2$. The parameters are the same as in figure 24, which corresponds to a threshold deviation $Re - Re_2 = -9$ for a ring with $\pi D/d = 59.0$. This is why the transition is very fast.

first amplified and lead to a long-wavelength modulation of the initial spanwise pattern. Furthermore, for $q \rightarrow 0$ the perturbation becomes a pure phase mode (Kuramoto 1984). For the bluff body wakes this translates into a growing waviness of the wake vortices, as illustrated by the numerical simulation shown in figure 27 (see also Leweke *et al.* 1993*b*).

The quantitative result for the stability limits of the ring wake modes is

$$Re_n = Re_c + \frac{4\pi^2(\mu/\nu)}{k(\pi D/d)^2}\left[\frac{3+c_1 c_2+2c_2^2}{1+c_1 c_2}\right]n^2, \tag{5.12}$$

i.e. their distance to the threshold Re_c of the primary instability is proportional to the square of the mode number and inversely proportional to the square of the aspect ratio. This result is plotted as solid lines in figures 4 and 14 for the values of the parameters given in (5.2) and the measured critical Reynolds numbers and aspect ratios in table 1. The dashed line in figure 4 represents the marginal stability limit of the plane waves, i.e. for a given Reynolds number it marks the winding number (proportional to the spanwise wavenumber), for which the amplitude (5.4*a*) of the (unstable) oscillation falls to zero. In expression (5.12) finite-size effects due to the periodic (and not infinite) domain are neglected. These effects slightly shift the instability boundary to lower Reynolds numbers. A calculation analogous to the one by Tuckerman & Barkley (1990) for a GL equation with real coefficients shows that in the present case these effects are smaller than the experimental uncertainty: a shift of about 1 in Reynolds number for the ring with aspect ratio 59.0, for example (Leweke 1994).

For the quantitative evaluation of the amplification rates α_n and frequencies ω_n of the Eckhaus instability, however, the finite spanwise size of the body is important, because they both depend on the perturbation wavenumber q (see the Appendix). Just like the initial plane waves, the perturbations can also only have discrete, and therefore finite wavenumbers $q_m = 2m/D$. The smallest value not equal to zero is q_1, which leads to the following expressions:

$$\frac{\partial}{\partial Re}\left(\alpha_n \frac{d^2}{\nu}\right)_{Re_n} = -\frac{(1+c_1 c_2)^2}{2(1+c_2^2)}\frac{k}{n^2}, \tag{5.13}$$

$$\omega_n \frac{d^2}{\nu} = 8\pi^2 \frac{(\mu/\nu)}{(\pi D/d)^2}(c_1 - c_2)\,n. \tag{5.14}$$

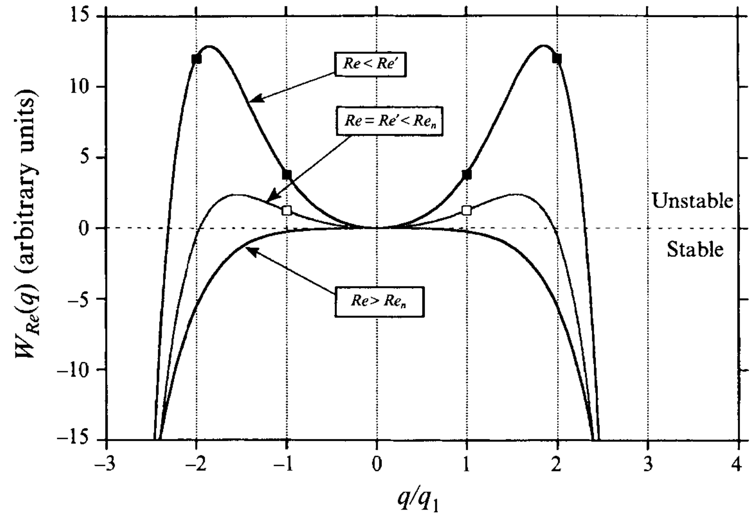

FIGURE 28. Qualitative shape of the stability function $W_{Re'}$ as function of the perturbation wavenumber, for a given helical mode. For small threshold deviations only the first discrete perturbation mode is unstable (□). For greater ΔRe (■) higher modes become unstable and dominate because of their higher amplification rate.

Since the growth rate is always zero at the instability limit (the definition of the latter), only its derivative (5.13) is of interest. It depends on the mode number, but not on the aspect ratio. The perturbation frequency is linear in mode number and inversely proportional to the square of the aspect ratio, but does not depend on Reynolds number. The agreement with the experimental data from the ring with $\pi D/d = 59.0$ in figures 16 and 17, always using the same model parameters (5.2), is very good.

The predictions of the Ginzburg–Landau model go even further in detail concerning this secondary instability in ring wakes. In the Appendix a stability function $W_{Re}(q)$ is defined, which qualitatively represents the growth rate of perturbations with wavenumber q. Figure 28 shows this function for several Reynolds numbers around a given Eckhaus limit Re_n. For $Re > Re_n$ all perturbations are damped, except the one with $q = 0$, which is always marginally stable. As soon as $Re < Re_n$ there exists an interval of unstable q around $q = 0$, with the size of this interval increasing with the threshold deviation $Re_n - Re$. First, this illustrates the finite-size effect on the stability limit. The initial solution remains stable until the unstable q-interval includes the first possible perturbation wavenumber q_1. In an infinite domain, infinitesimal q are possible, and the initial mode is destabilized as soon as $Re < Re_n$. But what is more interesting is the fact that, if the Reynolds number is decreased sufficiently far below the limit Re_n, the second discrete perturbation mode q_2 becomes unstable, and with a much higher growth rate than the first. If the transient of the Reynolds number change is sufficiently short this second mode should then 'win' over the first, or at least be clearly visible. In the Appendix it is shown that the perturbation frequency (the imaginary part of expression (A 8)) is proportional to the perturbation wavenumber, which gives a simple means to detect the nature of the most unstable perturbation. Figure 29 shows two experimental records of the phase fluctuations during the Eckhaus destabilization of mode 3 in the $\pi D/d = 76.2$ ring wake. The first in figure 29(*a*) was obtained for a Reynolds number just below the instability limit and the frequency is the one predicted by (5.14). In figure 29(*b*) the distance to Re_n is much greater and the basic

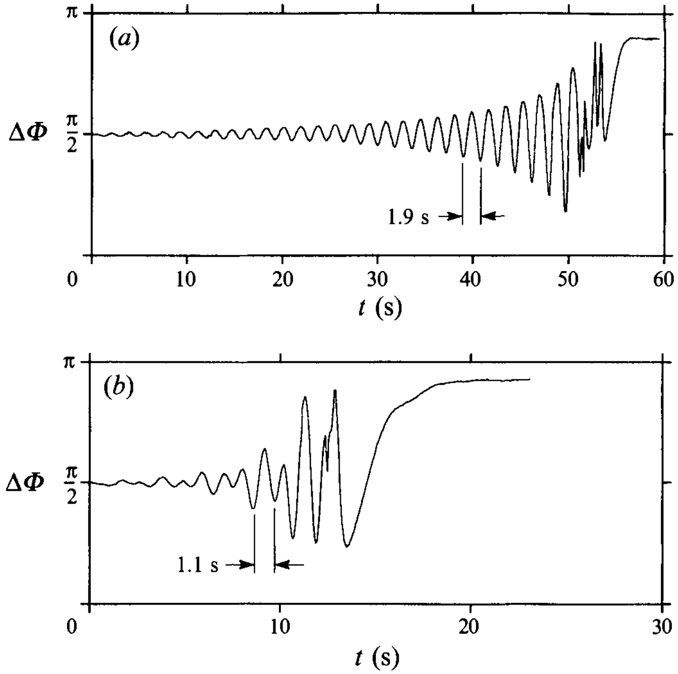

FIGURE 29. Development of the Eckhaus instability of mode $n = +3$ (compare figure 15), after step changes in Re: (*a*) $Re - Re_n = -1.5$, (*b*) $Re - Re_n = -5$. Ring with $\pi D/d = 76.2$. In (*b*) the final Reynolds number is much further away from the threshold than in (*a*), which results in a phase fluctuation frequency almost twice as high as in (*a*). This behaviour is predicted by the GL model.

frequency of the fluctuations is almost twice as high as before, which confirms the prediction of the GL model.

With the results shown in this section, it may be concluded that the Ginzburg–Landau model accounts qualitatively and quantitatively for all relevant experimental results concerning the secondary instability described in §3.4 and clearly identifies it as the Eckhaus instability of the *spanwise* pattern of vortex shedding. This must not be confused with a modulational instability of the *streamwise* vortex street pattern. The vortex street is more or less only a time recording of the near-wake dynamics and the downstream coordinate does not appear in the present model. Two-dimensional GL models including this direction have been studied numerically by Park & Redekopp (1992) and analytically by Chiffaudel (1992), who evokes a similar instability.

6. The Ginzburg–Landau model. II. The transition range

The results from the Ginzburg–Landau model presented in this section are more qualitative and less quantitative than the previous ones concerning the periodic regime. As shown above, the parameters of the model turn out to be more or less constant in the range $50 < Re < 100$ (except σ, of course), and their values can be determined with sufficient accuracy. One way to account for the deviations from this behaviour for higher Reynolds numbers is to allow for variable model parameters in equation (5.1). This, of course, requires that the model still has some kind of validity in this domain. The results presented in this section seem to confirm this assumption.

Equation (A 1) in the Appendix shows that the dynamical properties of the GL amplitude A are mainly determined by the parameters c_1 and c_2, c_0 represents a simple

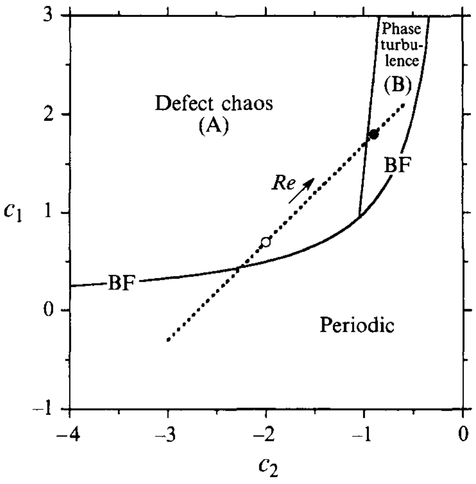

FIGURE 30. Parameter space for the Ginzburg–Landau model (following Shraiman *et al.* 1992) and trajectory (· · · · ·) for the transition regime according to (6.1). The symbols show the combinations used to obtain figures 31 (*a*) (○) and 31 (*b*) (●).

frequency shift and the remaining coefficients are just scaling factors. Here, the following variations of c_1 and c_2 are proposed for $Re > 100$:

$$c_1 = c_2 + 2.7, \quad c_2 = -4.1 + 0.011\,Re. \tag{6.1}$$

Actually, very little is known about the real values in this range and (6.1) was mainly chosen for its simplicity. However, it is sufficient to illustrate the main qualitative results, and the true evolution of these parameters is believed to be not fundamentally different from the one given here.

Figure 30 shows the trajectory described by (6.1) in the (c_1, c_2)-plane. At $Re = 100$ it starts off at the approximate value found for lower Reynolds numbers and then traverses a region where all periodic solutions (5.3) are unstable (see the Appendix): the Benjamin–Feir unstable domain with $1 + c_1 c_2 < 0$, above the line marked BF in figure 30. Recent numerical simulations performed by Shraiman *et al.* (1992) showed that this region is essentially divided into two parts corresponding to two different dynamical behaviours of the solutions of the Ginzburg–Landau equation: 'defect chaos' and 'phase turbulence'. The former is characterized by space–time dislocations, i.e. local phase jumps at low amplitude, and a small correlation length; the latter by the absence of dislocations and a much higher spatial correlation. This is illustrated by the spatio-temporal plots in figure 31 for the parameter combinations marked in figure 30. These two regimes are here associated with the vortex shedding modes A and B of the transition range, discussed in §4.

The plots in figure 31, however, can no longer be interpreted as a visualization of the real wake, as in the laminar regime. As shown by Williamson (1992), vortex dislocations in the transition range are complicated large-scale structures which spread in the spanwise direction as they travel downstream. Figure 31 (*a*) shows a time record of the near-wake spatial structure, i.e. of the beginning of the large-scale structure. It has to be remembered that the real wake is made up of vortical structures. Far from the body their evolution is governed by mechanisms, such as Biot–Savart induction, that are completely different from the near-wake dynamics modelled by the Ginzburg–Landau equation. Another 'downstream' effect in this Reynolds number

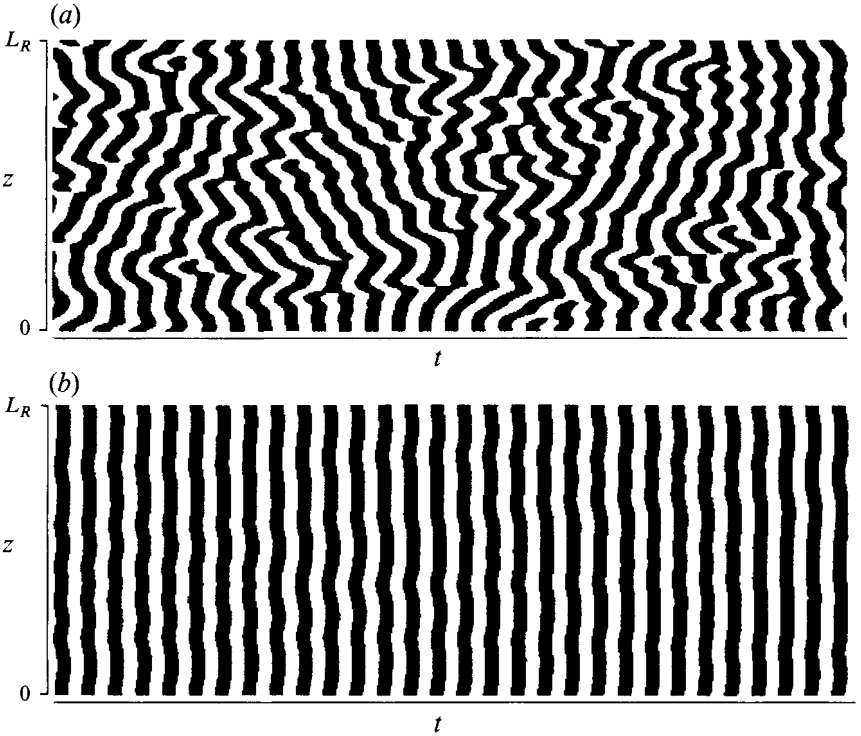

FIGURE 31. Spatio-temporal plots of the two characteristic behaviours in the Benjamin–Feir unstable domain. $L_R = 100$. (*a*) Defect chaos, $c_1 = 0.7$, $c_2 = -2.0$; (*b*) phase turbulence, $c_1 = 1.8, c_2 = -0.9$.

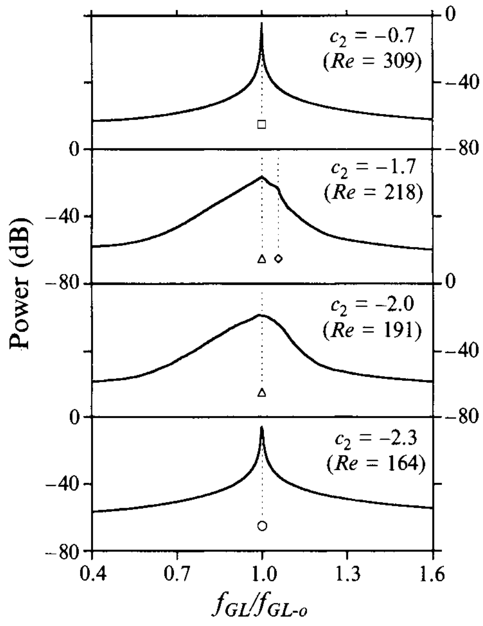

FIGURE 32. Time spectra of the GL amplitude A, obtained from numerical simulations of (5.1) with parameters (5.2*a–d*) and (6.1), and $L_R = 100$. Symbols as in figure 20.

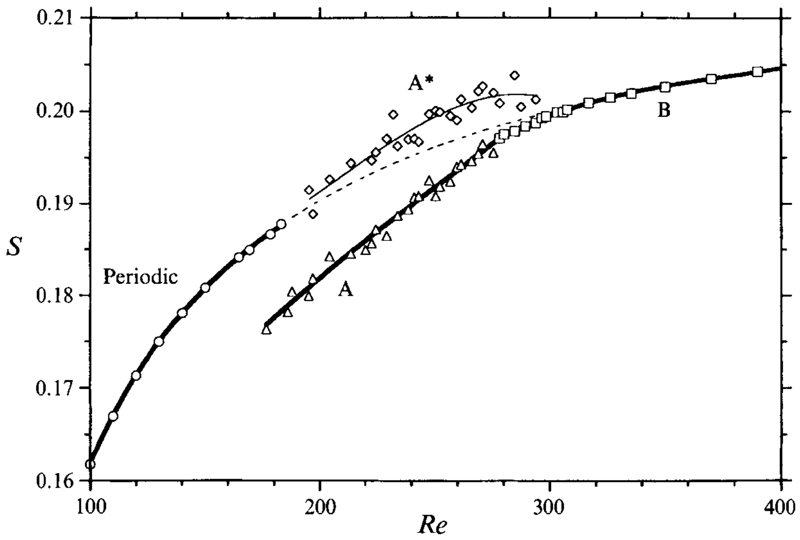

FIGURE 33. S–Re relationship resulting from the GL model. For a given c_2, the Reynolds number was calculated from (6.1), and the Strouhal number from (6.2). Symbols as in figure 20. The dashed line marks the frequency of the parallel plane wave solutions, which become unstable beyond the Benjamin–Feir instability limit.

range is the transition to turbulent motion observed some distance from the body and which is initiated by the three-dimensional near-wake perturbations and their downstream evolution.

The qualitative comparisons between the Ginzburg–Landau model and real bluff body wakes in the transition regime can be made more quantitative by determining the Strouhal–Reynolds number relationship for the GL model. This was done using numerical simulations of the GL equation in non-dimensional form (A 1) and the coefficients (6.1), but without the frequency shift in (A 2*c*). For the coefficient c_0 of the linear oscillation frequency, expression (5.2*d*) from the laminar range was continued across the transition regime with a linear variation of Ro_0 with Reynolds number, close to typical bluff body results. As shown in figure 32 the time spectra of the calculated solution A are very similar to the experimentally determined velocity spectra in figure 20. The Strouhal number was calculated from the dimensionless frequency f' in the same way as illustrated in figure 20 and using the relation

$$S = \frac{k}{2\pi} f' \frac{Re - Re_c}{Re}, \tag{6.2}$$

which results from (A 2*d*), (5.2*a*) and $S = (fd^2/\nu)/Re$.

The result is shown in figure 33 for a dimensionless domain length $L_R = 100$ (see (A 2*b*)) and periodic boundary conditions. It shows a strong resemblance to the experimental result for the ring wake shown in figure 2(*a*). In the periodic domain, the oscillation frequency has the value of the plane wave solution given by (5.7) (dashed line). When the Benjamin–Feir stability limit is passed at $Re \approx 180$ and the region of defect chaos is entered, the principal frequency drops to lower values. Shraiman *et al.* showed that when the limit is passed in the other direction, by varying the parameters in a single run, the defect chaos mode persists in the Benjamin–Feir stable range, or is at least a long-lived transient. This is very close to the hysteretic behaviour of the ring or straight cylinder wakes described in §4. The difference between observed and plane

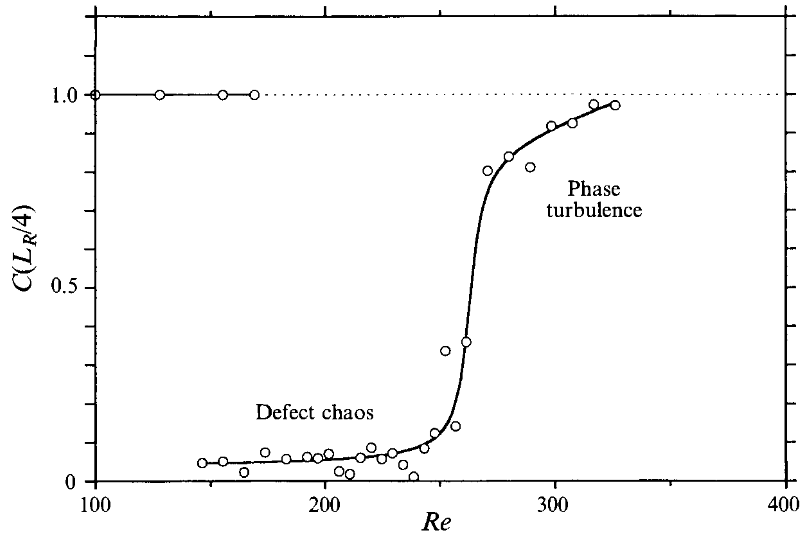

FIGURE 34. Coefficient of spatial correlation, obtained from simulations of the Ginzburg–Landau model, for the fluctuations at points separated by one quarter of the domain size L_R.

wave frequencies then reduces as the domain of phase turbulence is approached, and no discontinuity occurs during the transition to this mode. The discontinuity in the slope of the Strouhal curve is less pronounced than in the experiments. A third transition mode, which corresponds to mode A* in the ring wake, also appears, with a weak side peak in the spectra at frequencies higher than the plane wave frequency (figure 32, $c_2 = -1.7$).

Another comparison is possible between the spatial correlation functions. The correlation coefficient C defined by (4.1) was calculated for $\Delta z = L_R/4$ from the numerical results; it is shown in figure 34. The sharp drop from the perfect correlation in the periodic mode to very small values in the defect chaos mode (A) and the subsequent fast increase during the transition to the phase turbulence mode (B) are very similar to the results seen in figure 23. However, the correlation coefficient climbs to much higher values in the model than in the real wake, and if the trajectory in parameter space in figure 30 and (6.1) was extended to higher Reynolds numbers it is clear that C would reach the value 1 again when the Benjamin–Feir unstable range is left. In real bluff body wakes it is the increase of the small-scale perturbations in the form of streamwise vortices which makes the spanwise correlation (as in figure 23) decrease again for higher Reynolds numbers. These streamwise vortices of mode B are believed to be the result of a centrifugal instability of the Kármán vortices in the near-wake formation region (see e.g. König 1993 and Zhang, Noack & Eckelmann 1994). Such a mechanism can obviously not be reproduced by the simple Ginzburg–Landau model, which explains the differences between model and experiment concerning the spanwise correlation, and also the 'background' noise level in the spectra, in this Reynolds number range.

Considering the very simplified choice of the GL parameter variation (6.1), the agreement between model and reality, concerning oscillation spectra, frequencies, and correlation functions, is very good. Experimental phenomena, such as the hysteresis at the transition between periodic mode and defect chaos, widening of the peaks in the oscillation spectra, 'double peaks' in the spectra, or discontinuities in the Strouhal curves, appear naturally in the Ginzburg–Landau model as consequences of the Benjamin–Feir instability, and this for a completely smooth variation of the model parameters.

7. Discussion and conclusions

In this study, precise experimental results concerning the wakes behind bluff rings at low Reynolds numbers were obtained. These are compared to the predictions of a simple dynamical wake model involving a Ginzburg–Landau equation. The combination of the two give a number of new insights into the behaviour of bluff body wakes in general.

First of all, the validity of the phenomenological approach consisting of the interpretation of bluff body wakes in terms of amplitude equations is further confirmed. For this kind of open flow, this concept was first applied to straight circular cylinder configurations, but the comparison with experiments remained rather qualitative, especially concerning three-dimensional phenomena. This is not too surprising because an important part of these flows, the one close to the body ends, cannot be accurately incorporated in such a simple model. In the present ring geometry, end effects are absent and the Ginzburg–Landau model can become fully operational. The good quantitative agreement between experimental and analytical results presented in this paper reflects this. The body curvature, which is present in the experiments, but does not appear in the model, is shown to add only small quantitative changes.

Furthermore, the present model turns out to be more than just a truncated development of the Navier–Stokes equations near the onset of the Bénard–von Kármán instability. With constant coefficients it is valid up to $Re = 100$, and when allowing for a variation of the parameters it describes the wake dynamics up to Reynolds numbers of the order of 300 or more.

The ring wake results and the Ginzburg–Landau model applied to a bluff body of infinite length can also give answers to the question of which phenomena are intrinsic to the wakes behind such idealized bodies and which are linked to specific end configurations. One of these phenomena is oblique vortex shedding. Although it is influenced by end effects, it is nevertheless an intrinsic feature of the infinite-cylinder problem. As shown by the solutions (5.3), a whole band of spanwise wavenumbers, i.e. oblique shedding angles, centred around $Q = 0$ is possible, limited only by the Eckhaus instability. In a periodic domain like the ring wake, obviously only discrete values are allowed. In recent experimental studies, König, Noack & Eckelmann (1993) and Brede *et al.* (1994) also reported on discrete shedding modes in the wake of a straight cylinder, which seems to be in contradiction with the expected continuum of shedding angles. It is believed, however, that this discreteness is the result of an interaction between the main body of the wake and the lower-frequency end cells. When there are no such cells, as e.g. in the experiments of Miller & Williamson (1994) or below $Re \approx 65$ in König *et al.* (1993), a continuum of angles is observed. This suggests that discrete shedding modes in cylinder wakes are a product of a particular set of end conditions (which are also the most commonly used), and not an intrinsic feature of the wakes behind infinitely long cylinders. The same applies to related phenomena, such as additional spanwise cells of different frequencies, quasi-periodic velocity signals, discontinuities in the periodic shedding frequency, and transitions between different shedding angles. For infinite or ring geometries, the only stable asymptotic solutions in the periodic regime are the plane waves described by (5.3); everything else is due to end effects.

As a consequence of the absence of the predominating influence of the ends, new, more subtle phenomena can be observed in the ring wake. This is the case for the Eckhaus instability described in §3.4. The ring geometry allows for the first time the quantitative study of this secondary instability in an open flow system. For this the Ginzburg–Landau model is of great help in clearly identifying the observed phenomena, without which they would have remained somewhat mysterious. Since the curvature of the rings does not appear in the model, the Eckhaus instability should also occur in the wake of straight circular cylinders. It is probably at the origin of the transition between different oblique shedding modes and the formation of spanwise cells of different shedding frequencies described by Williamson (1988*a*) and König *et al.* (1990). These phenomena are associated with discontinuities in the Strouhal curve and they are believed to occur whenever the oblique angle induced by the end configuration exceeds the Eckhaus limit. As discussed in §5.3 and in more detail in Leweke (1994), this limit is an increasing function of Reynolds number, approximately proportional to $(Re-Re_c)^{1/2}$, which agrees well with the maximum values of the shedding angles observed by König *et al.* (1993, figure 1).

Another set of results concerns the transition range. Once it is established that laminar bluff body wakes behave like a one-dimensional chain of diffusively coupled oscillators, whose dynamics are described by a Ginzburg–Landau equation, and the parameters of this equation are approximately known, it is only a small step to identify the instability of the periodic wake as the Benjamin–Feir instability, which is a well-known feature of this equation. A comparison with experiments, however, is only possible by eliminating the end effects, which cannot be correctly modelled, by the use of the ring geometry. In §4 these effects are shown to cause important qualitative changes in the transition dynamics, especially a second Strouhal discontinuity, not found in the ring wakes. The intriguing behaviour of the experimental spectra in figure 20 and of the Strouhal curve in figure 21(*a*) is then qualitatively explained by the passage of the Ginzburg–Landau parameters through the Benjamin–Feir unstable domain, even if the exact variation of these parameters with Reynolds number and their precise physical interpretation are not known for the moment. The good agreement between ring wake and model also shows that the difference in the transition behaviour between cylinders and rings is not due to the body curvature. Two- and three-dimensional numerical simulations could help in finding the model parameters for Reynolds numbers close to the transition range, since the necessary experiments seem quite impossible, even for the 'clean' ring geometry.

It is known for circular cylinders that the Reynolds number Re_t, where the periodic vortex shedding becomes unstable, is sensitive to experimental conditions, such as turbulence level or end configurations. Therefore it could not yet be determined with certainty if parallel shedding has a higher transition Reynolds number than oblique shedding or vice versa. The ring wake results seem to suggest that inclined modes are more stable than the parallel mode (figure 18). However, with the parameter variation (6.1) proposed for the transition range, the Ginzburg–Landau model predicts a longer stability of the parallel mode, so that the experimental result may be linked to the body curvature. Even if the effect of the latter is small, it may be sufficient to influence this sensitive transition. The question concerning the transition Reynolds numbers of oblique and parallel vortex shedding in the wake of an infinite cylinder therefore remains open, at least until a precise knowledge of the Ginzburg–Landau parameters is available.

It is important to notice that the transition range is a succession of completely different physical phenomena occurring in the near-wake formation region behind the body. The first is a dynamical instability, the Benjamin–Feir instability at $Re_t \approx$ 180–200, of the essentially one-dimensional (spanwise) system of fluid-dynamical oscillators, which the near wake represents. The resulting chaotic motion of mode A in the near wake is not what would be characterized as turbulence, i.e. fluctuations in large scale, velocity and frequency ranges. The more turbulent motion observed further downstream is only a secondary effect, initiated by the three-dimensional distortion of the vortices (Williamson 1991, 1992). The second phenomenon is the appearance at $Re \approx 220$ of small-scale counter-rotating streamwise vortices, presumably as a consequence of a centrifugal instability of the Kármán vortices in the near wake (König 1993; Zhang *et al.* 1994). This is superimposed on the dynamics of the one-dimensional system described by the Ginzburg–Landau equation. Finally the separated shear layer instability sets in at $Re \approx 1000$ with the appearance of the spanwise Kelvin–Helmholtz vortices.

These three phenomena appear to be *a priori* uncorrelated and it may be a particular feature of the circular-cross section body that they happen in this particular order.

Up to today, perhaps more than 99% of the experimental results concerning bluff body wake dynamics at low Reynolds numbers have been obtained from studies of straight cylinders with ends, mostly of circular cross-section. However, with the recent recognition of the dominating influence of end effects, which is further emphasized by the present study, the ring geometry may be a more useful configuration to study intrinsic wake phenomena, even with the slight modifications introduced by curvature and the undoubtedly more complicated experimental setup.

The authors are grateful to Louis Boyer and Pierre Albarède for many valuable discussions. Special thanks are due to Charles Williamson for his continued interest in this study and his suggestions, especially concerning the transition regime. The authors are also grateful to Alain Pocheau and Pierre Pelcé for discussions about the Ginzburg–Landau model, and to Michael König and Bernd Noack. Lastly, the authors thank François Abetino and René DelPapa for their technical assistance, and Jacky Minelli for his patience with the manufacture and repair of the ring models. The partial financial support from the Groupement de Recherche 'Ordre et Chaos dans la Matière' of the French CNRS, and from the French Ministère de l'Enseignement Supérieur et de la Recherche 'Action Incitative du D.S.P.T. 8 en Mécanique des Fluides' is gratefully acknowledged.

Appendix. Analytical treatment of the Eckhaus and Benjamin–Feir instabilities

The analysis in this section follows the study of Kuramoto (1984) and the results are derived for an infinite domain only. The Ginzburg–Landau equation (5.1) and its solutions (5.3) can be put in the dimensionless standard form

$$\frac{\partial A'}{\partial t'} = A' + (1+\mathrm{i}c_1)\frac{\partial^2 A'}{\partial z'^2} - (1+\mathrm{i}c_2)\,|A'|^2 A' \tag{A 1}$$

by the following transformations (Albarède 1991):

$$t' = t\sigma, \quad z' = z(\sigma/\mu)^{1/2}, \tag{A 2a, b}$$

$$A' = A(l/\sigma)^{1/2}\exp(-\mathrm{i}c_0\,\sigma t), \tag{A 2c}$$

$$\Omega' = \Omega/\sigma, \quad Q' = Q(\mu/\sigma)^{1/2}. \tag{A 2d, e}$$

Inserting the non-dimensionalized version of (5.10) in (A 1) and linearizing yield the evolution equations for the (already non-dimensional) perturbations a and ϕ:

$$\frac{\partial a}{\partial t'} = \frac{\partial^2 a}{\partial z'^2} - 2Q'c_1\frac{\partial a}{\partial z'} - 2(1-Q'^2)\,a - c_1\frac{\partial^2 \phi}{\partial z'^2} - 2Q'\frac{\partial \phi}{\partial z'}, \tag{A 3a}$$

$$\frac{\partial \phi}{\partial t'} = \frac{\partial^2 \phi}{\partial z'^2} - 2Q'c_1\frac{\partial \phi}{\partial z'} + c_1\frac{\partial^2 a}{\partial z'^2} + 2Q'\frac{\partial a}{\partial z'} - 2c_2(1-Q'^2)\,a. \tag{A 3b}$$

Choosing perturbations in the form of Fourier modes (5.11) these equations can be rewritten as

$$\Lambda'\begin{pmatrix} a_0 \\ \phi_0 \end{pmatrix} = \begin{pmatrix} -q'^2 - 2\mathrm{i}c_1 Q'q' - 2(1-Q'^2) & c_1 q'^2 - 2\mathrm{i}Q'q' \\ -c_1 q'^2 + 2\mathrm{i}Q'q' - 2c_2(1-Q'^2) & -q'^2 - 2\mathrm{i}c_1 Q'q' \end{pmatrix}\begin{pmatrix} a_0 \\ \phi_0 \end{pmatrix}. \tag{A 4}$$

The equation for the eigenvalues Λ' is

$$\Lambda'^2 + (a_1 + \mathrm{i}a_2)\,\Lambda' + (b_1 + \mathrm{i}b_2) = 0 \tag{A 5}$$

with coefficients

$$\left.\begin{aligned} &a_1 = 2(1-Q'^2+q'^2), \quad a_2 = 4c_1 Q'q', \\ &b_1 = (1+c_1^2)(q'^2-4Q'^2)\,q'^2 + 2(1+c_1c_2)(1-Q'^2)\,q'^2, \\ &b_2 = 4(c_1-c_2)(1-Q'^2)\,Q'q'. \end{aligned}\right\} \tag{A 6}$$

The exact eigenvalues are

$$\begin{aligned} \Lambda'_{\pm} = {} & -(1-Q'^2+q'^2) - 2\mathrm{i}c_1 Q'q' \pm [(1-Q'^2)^2 + (2Q'q')^2 \\ & - 2c_1c_2(1-Q'^2)\,q'^2 + 4\mathrm{i}c_2(1-Q'^2)\,Q'q' + 4\mathrm{i}c_1 Q'q'^3 - c_1^2 q'^4]^{1/2}. \end{aligned} \tag{A 7}$$

For the Eckhaus modulational instability ($q' \rightarrow 0$), only Λ'_+ is relevant, since $\Lambda'_- \rightarrow -2(1-Q'^2)$ in this limit, i.e. perturbations are damped for all possible values of $Q'(<1)$. For small q', Λ'_+ can be expanded into

$$\Lambda'_+ = -2\mathrm{i}(c_1-c_2)\,Q'q' - \left[(1+c_1c_2) - \frac{2(1+c_2^2)\,Q'^2}{1-Q'^2}\right]q'^2 + O(q'^3). \tag{A 8}$$

Instability occurs when the real part of this expression (the growth rate α, which is the second term on the right-hand side) becomes positive. This happens for

$$Q'^2 > Q_c'^2 = \frac{1+c_1c_2}{3+2c_2^2+c_1c_2}. \tag{A 9}$$

The stability limit found by setting $Q'^2 = Q_c'^2$. The result (5.12) for the ring wake is obtained by returning to dimensional and physical variables via (A 2*d*, *e*) and (5.2*a*) and by replacing Q by the discrete values Q_n. The expressions (5.13) and (5.14) for the frequency (the imaginary part in (A 8)) and the growth rate, respectively, are found in the same way and by choosing the smallest possible perturbation wavenumber $q = q_1$.

The function W of figure 28 is defined as

$$W \equiv b_2^2 - a_1a_2b_2 - a_1^2b_1, \tag{A 10}$$

with the relations (A 6) for the parameters. It is qualitatively equivalent to the growth rate α, and its expression is obtained for the condition that, at the stability limit, one of the eigenvalues Λ' in (A 5) is purely imaginary. For details see the discussion by Kuramoto (1984). The Reynolds number dependence enters via (A 2*e*) and (5.2*a*).

For the Eckhaus instability to occur, the spanwise wavenumber has to pass a critical value, the uniform oscillation, or parallel mode, always being stable. However, under different circumstances, this parallel mode can also become unstable. For $Q' = 0$ the stability function reduces to

$$W = -8(1+q'^2)^2 q'^2[1+c_1 c_2 + \tfrac{1}{2}(1+c_1^2)\, q'^2]. \tag{A 11}$$

The stability of the uniform oscillation is now governed by the sign of the expression $1+c_1 c_2$. For positive values, W is negative for all perturbation wavenumbers q', implying stability. As soon as $1+c_1 c_2 < 0$, there exist finite q' close to zero for which W becomes positive. In the latter case all plane wave solutions are unstable, not just the ones with $Q' > Q'_c$ as for the Eckhaus case discussed above. This is the Benjamin–Feir instability. The mechanism by which the uniform oscillation is destabilised is very similar to the Eckhaus case, i.e. by long-wavelength phase modulations due to the resonant excitation of sideband disturbances. However, their exponential growth is not accompanied by phase oscillations, since the corresponding eigenvalue has no imaginary part (Kuramoto 1984). Under certain approximations the quantity $1+c_1 c_2$ may be interpreted as the diffusion coefficient for the phase of A' (Kuramoto 1984), and it is intuitively clear that a negative diffusion coefficient leads to a (violent) instability.

REFERENCES

Albarède, P. 1991 Self-organization in three-dimensional wakes of bluff bodies. PhD thesis, Université de Provence, Marseille, France.

Albarède, P. & Monkewitz, P. A. 1992 A model for the formation of oblique shedding patterns and 'chevrons' in cylinder wakes. *Phys. Fluids* A **4**, 744.

Albarède, P. & Provansal, M. 1995 Quasi-periodic cylinder wakes and the Ginzburg–Landau model. *J. Fluid Mech.* (To appear).

Albarède, P., Provansal, M. & Boyer, L. 1990 The Ginzburg–Landau equation as a model for the three-dimensional wake of an elongated bluff body. *C. R. Acad. Sci. Paris* **310** (II), 459.

Bearman, P. W. & Takamoto, M. 1988 Vortex shedding behind rings and disks. *Fluid Dyn. Res.* **3**, 214.

Berger, E. & Wille, R. 1972 Periodic flow phenomena. *Ann. Rev. Fluid Mech.* **4**, 313.

Bloor, S. 1964 The transition to turbulence in the wake of a circular cylinder. *J. Fluid Mech.* **19**, 290.

Brede, M., Eckelmann, H., König, M. & Noack, B. R. 1994 Discrete shedding modes of the cylinder wake in a jet with a homogeneous core. *Phys. Fluids* **6**, 2711.

Chiffaudel, A. 1992 Non-linear stability analysis of two-dimensional patterns in the wake of a circular cylinder. *Europhys. Lett.* **18**, 589.

Coutanceau, M. & Defaye, J.-R. 1991 Circular cylinder wake configurations: a flow visualisation survey. *Appl. Mech. Rev.* **44**, 255.

Cross, M. C. & Hohenberg, P. C. 1993 Pattern formation outside of equilibrium. *Rev. Mod. Phys.* **65**, 851.

Ehrhardt, G. 1979 Stabilität zweireihiger Straßen geradliniger und kreisförmiger Wirbel. *Fortschrittsber. der VDI-Z.*, Reihe 7, no. 49.

Eisenlohr, H. & Eckelmann, H. 1989 Vortex splitting and its consequences in the vortex street wake of cylinders at low Reynolds number. *Phys. Fluids* A **1**, 189.

Gaster, M. 1969 Vortex shedding from slender cones at low Reynolds numbers, *J. Fluid Mech.* **38**, 565.

Gaster, M. 1971 Vortex shedding from circular cylinders at low Reynolds numbers. *J. Fluid Mech.* **46**, 749.

Gerich, D. & Eckelmann, H. 1982 Influnce of end plates and free ends on the shedding frequencies of circular cylinders. *J. Fluid Mech.* **122**, 109.

GERRARD, J. H. 1978 The wakes of cylindrical bluff bodies at low Reynolds number. *Phil. Trans. R. Soc. Lond.* A **288**, 351.

GOUJON-DURAND, S., JENFFER, P. & WESFREID, J. E. 1994 Downstream evolution of the Bénard–von Kármán instability. *Phys. Rev.* E **50**, 308.

HAMA, F. R. 1957 Three-dimensional vortex pattern behind a circular cylinder. *J. Aero. Sci.* **24**, 156.

HAMMACHE, M. & GHARIB, M. 1989 A novel method to promote parallel shedding in the wake of circular cylinders. *Phys. Fluids* A **1**, 1611.

HAMMACHE, M. & GHARIB, M. 1991 An experimental study of the parallel and oblique vortex shedding from circular cylinders. *J. Fluid Mech.* **232**, 567.

HUERRE, P. & MONKEWITZ, P. A. 1990 Local and global instabilities in spatially developing flows. *Ann. Rev. Fluid Mech.* **22**, 473.

JANIAUD, B., PUMIR, A., BENSIMON, D., CROQUETTE, V., RICHTER, H. & KRAMER, L. 1992 The Eckhaus instability for traveling waves. *Physica* D **55**, 269.

KARNIADAKIS, G. E. & TRIANTAFYLLOU, G. S. 1989 Frequency selection and asymptotic states in laminar wakes. *J. Fluid Mech.* **199**, 441.

KARNIADAKIS, G. E. & TRIANTAFYLLOU, G. S. 1992 Three-dimensional dynamics and transition to turbulence in the wake of bluff objects. *J. Fluid Mech.* **238**, 1.

KÖNIG, M. 1993 Experimentelle Untersuchung des dreidimensionalen Nachlaufs zylindrischer Körper bei kleinen Reynoldszahlen. *Mitt. Max-Planck-Institut für Strömungsforschung* 111.

KÖNIG, M., EISENLOHR, H. & ECKELMANN, H. 1990 The fine structure in the Strouhal–Reynolds number relationship of the laminar wake of a circular cylinder. *Phys. Fluids* A **2**, 1607.

KÖNIG, M., NOACK, B. R. & ECKELMANN, H. 1993 Discrete shedding modes in the von Kármán vortex street. *Phys. Fluids* A **5**, 1846.

KRAMER, L. & ZIMMERMANN, W. 1985 On the Eckhaus instability for spatially periodic patterns. *Physica* **16D**, 221.

KURAMOTO, Y. 1984 *Chemical Oscillations, Waves, and Turbulence*, Appendix A. Springer.

LEWEKE, T. 1994 Experimental study and modelling of the wake of a ring at low Reynolds numbers. PhD thesis, Université de Provence, Marseille, France.

LEWEKE, T. & PROVANSAL, M. 1994*a* Model for the transition in bluff body wakes. *Phys. Rev. Lett.* **72**, 3174.

LEWEKE, T. & PROVANSAL, M. 1994*b* Determination of the parameters of the Ginzburg–Landau wake model from experiments on a bluff ring. *Europhys. Lett.* **27**, 655.

LEWEKE, T., PROVANSAL, M. & BOYER, L. 1993*a* Three-dimensional wake of a torus and its modelling by the Ginzburg–Landau equation. *C. R. Acad. Sci. Paris* **316** (II), 287.

LEWEKE, T., PROVANSAL, M. & BOYER, L. 1993*b* Stability of vortex shedding modes in the wake of a ring at low Reynolds numbers. *Phys. Rev. Lett.* **71**, 3469.

LOWE, M. & GOLLUB, J. P. 1985 Pattern selection near the onset of convection: the Eckhaus instability. *Phys. Rev. Lett.* **55**, 2575.

MATHIS, C., PROVANSAL, M. & BOYER, L. 1984 The Bénard–von Kármán instability: an experimental study near the threshold. *J. Phys. Lett. (Paris)* **45**, L483.

MILLER, G. D. & WILLIAMSON, C. H. K. 1994 Control of three-dimensional phase dynamics in a cylinder wake. *Exps. Fluids* **18**, 26.

MONSON, D. R. 1965 Experimental drag characteristics of tori, ducted-spheres, and other shapes at low Reynolds numbers. Masters thesis, University of Minnesota.

MONSON, D. R. 1981 The effect of transverse curvature on the drag and vortex shedding of elongated bluff bodies at low Reynolds numbers. *ASME Paper* 81-WA/FF-4.

MONSON, D. R. 1983 The effect of transverse curvature on the drag and vortex shedding of elongated bluff bodies at low Reynolds numbers. *Trans. ASME* I: *J. Fluids Engng.* **105**, 308.

NOACK, B. R., KÖNIG, M. & ECKELMANN, H. 1993 Three-dimensional stability analysis of the periodic flow around a circular cylinder. *Phys. Fluids* A **5**, 1279.

NORBERG, C. 1994 An experimental investigation of the flow around a circular cylinder: influence of aspect ratio. *J. Fluid Mech.* **258**, 287.

PARK, D. S. & REDEKOPP, L. G. 1992 A model for pattern selection in wake flows. *Phys. Fluids* A **4**, 1697.

Provansal, M., Mathis, C. & Boyer, L. 1987 Bénard–von Kármán instability: transient and forced regimes. *J. Fluid Mech.* **182**, 1.

Rivet, J.-P. 1991 Spontaneous symmetry-breaking in the 3-D wake of a bluff cylinder, simulated by the lattice gas method. *C. R. Acad. Sci. Paris* **313** (II), 151.

Roshko, A. 1953 On the development of turbulent wakes from vortex streets. *NACA Tech. Note* 2913.

Saffmann, P. G. 1992 *Vortex Dynamics*, chap. 10. Cambridge University Press.

Schumm, M., Berger, E. & Monkewitz, P. A. 1994 Self-excited oscillations in the wake of two-dimensional bluff bodies and their control. *J. Fluid Mech.* **271**, 17.

Shraiman, B. I., Pumir, A., Saarlos, W. van, Hohenberg, P. C., Chaté, H. & Holen, M. 1992 Spatiotemporal chaos in the one-dimensional complex Ginzburg–Landau equation. *Physica* D **57**, 241.

Sreenivasan, K. R. 1985 Transition and turbulence in fluid flows and low-dimensional chaos. In *Frontiers in Fluid Mechanics* (ed. S. H. Davis & J. L. Lumley), pp. 41–66. Springer.

Sreenivasan, K. R., Strykowski, P. J. & Ohlinger, D. J. 1986 Hopf bifurcation, Landau equation and vortex shedding behind circular cylinders. In *Proc. Forum on Unsteady Flow Separation* (ed. K. N. Ghia), pp. 1–13, ASME.

Stuart, J. T. & DiPrima, R. C. 1978 The Eckhaus and Benjamin–Feir resonance mechanisms. *Proc. R. Soc. Lond.* A **362**, 27.

Takamoto, M. 1987 A study of the wake structure behind bluff rings. *Bull. NRLM (Japan)* **36**, 441.

Takamoto, M. & Izumi, K. 1981 Experimental observation of stable arrangement of vortex rings. *Phys. Fluids* **24**, 1582.

Tritton, D. J. 1959 Experiments on the flow past a circular cylinder at low Reynolds numbers. *J. Fluid Mech.* **6**, 547.

Tritton, D. J. 1971 A note on vortex streets behind circular cylinders at low Reynolds numbers. *J. Fluid Mech.* **45**, 203.

Tuckerman, L. & Barkley, D. 1990 Bifurcation analysis of the Eckhaus instability. *Physica* D **46**, 57.

Van Atta, C. W. & Gharib, M. 1987 Ordered and chaotic vortex streets behind circular cylinders at low Reynolds numbers. *J. Fluid Mech.* **174**, 113.

Williamson, C. H. K. 1988*a* Defining a universal and continuous Strouhal–Reynolds number relationship for the laminar vortex shedding of a circular cylinder. *Phys. Fluids* **31**, 2742.

Williamson, C. H. K. 1988*b* The existence of two stages in the transition to three-dimensionality of a circular cylinder wake. *Phys. Fluids* **31**, 3165.

Williamson, C. H. K. 1989 Oblique and parallel modes of vortex shedding in the wake of a circular cylinder at low Reynolds numbers. *J. Fluid Mech.* **206**, 579.

Williamson, C. H. K. 1991 Three-dimensional aspects and transition of the wake of a circular cylinder. In *Turbulent Shear Flows 7* (ed. F. Durst & J. Launder), pp. 173–194. Springer.

Williamson, C. H. K. 1992 The natural and forced formation of spot-like 'vortex dislocations' in the transition of a wake. *J. Fluid Mech.* **243**, 393.

Williamson, C. H. K. 1995 Vortex dynamics in the wake of a cylinder. In *Fluid Vortices* (ed. S. Green). Kluwer Academic (to appear).

Williamson, C. H. K. & Roshko, A. 1990 Measurements of base pressure in the wake of a cylinder at low Reynolds numbers. *Z. Flugwiss. Weltraumforsch.* **14**, 38.

Zhang, H.-Q., Noack, B. R. & Eckelmann, H. 1994 Numerical computation of the 3-D cylinder wake. *Rep. 3/1994*. Max-Planck-Institut für Strömungforschung, Göttingen.